UiT The Arctic University of Norway

Faculty of Science and Technology
Department of Physics and Technology

Dual Radar Detections of Meteors Using Calibrated EISCAT UHF Data

Sara Våden

FYS-3931 Master's thesis in Space Physics 30 SP
31 May 2024

This thesis document was typeset using the *UiT Thesis LaTeX Template*.
© 2024 – http://github.com/egraff/uit-thesis

Abstract

The atmosphere of Earth experiences a continuous entry of particles of various sizes originating from several sources. Meteoroids, which are called meteors when entering the atmosphere, are particles that can be measured by radars through scattering off the meteor head plasma which forms around the meteor. These measurements can give information on the processes the meteor undergoes as it travels through the atmosphere.

The work in this thesis provides a timing calibration of the EISCAT UHF system for meteor studies, calculates the RCS of meteor head echoes using an accurate EISCAT UHF beam pattern and the MAARSY-derived meteor location, proposes and presents a method by which to detect and classify simple ablation, differential ablation, and fragmentation meteor events, and considers the results from this analysis in the context of previous research.

Differential ablation was most successfully classified through the method developed, while simple ablation and fragmentation were more ambiguous. The analysis of differential ablation meteor events shows a clear drop in the radar signal at approximately 100 km altitude, indicating the complete ablation of, for example, Na and K particles in the meteor. A case study of a meteor undergoing fragmentation shows the signature oscillatory pattern originating from two or more fragments moving with different velocities.

Acknowledgements

First and foremost, I would like to give a big thank you to my supervisor Devin Huyghebaert for introducing me to the many interesting aspects of this topic. Your guidance, prompt feedback, and constant willing to help have been extremely useful. This work has been incredibly interesting, and I have learned a great deal for which I am very grateful.

I would also like to thank my co-supervisor Juha Vierinen for assisting with the alignment of EISCAT and MAARSY data, processing of the MAARSY data and for letting me borrow your server for the processing and calculations.

I am deeply grateful to my family for their constant support that got me through the last five years. Lastly, I would like to thank Brian for proofreading this thesis and keeping me motivated these past months.

Contents

List of Figures

List of Tables

1 Introduction

Every day, a large number of particles of various sizes enter the Earth's atmosphere. These particles originate from different sources as asteroids, comets and meteoroids. As they travel through space, the particles can be called cosmic dust. They can change sizes through collisions or sublimation due to an increase in temperature. When meteoroid particles, having sizes between $10^{-4}\mu g$ and 100 g, enter the Earth's atmosphere, they are called meteors (Limonta et al., 2020). These meteors undergo processes on their trajectory towards Earth's surface that cause them to release metallic particles, which have an impact on the atmosphere.

One of these processes is called ablation and is caused by a greater aerodynamic pressure than the material strength holding the meteor together. From this pressure, heat is generated and the different constituent elements of the meteor will evaporate. The components have different heat resistances and therefore evaporate at different altitudes. The meteor can also experience fragmentation while it is moving through the atmosphere. Fragmentation is when a meteor breaks into two or more separate pieces that do not evaporate completely. As these pieces originate from the same parent body, they will have similar velocities and trajectories shortly after the fragmentation. However, the pieces have different masses, shapes and small differences in their velocity which cause them to start drifting apart from each other (Malhotra and Mathews, 2011). Through the use of radar observations, this thesis investigates ablation and fragmentation of meteors.

Due to the ability to observe meteors within a large mass range, radar observation is one of the most common techniques to measure meteors traveling through the atmosphere. In this work, radar data is used from two different radars with two different frequencies: EISCAT UHF at 930 MHz and MAARSY at 53.5 MHz. These radars both operated during the 2023 Geminids meteor shower, enabling dual detection of meteor events. Tarnecki et al. (2021) and Schult et al. (2021) have conducted previous studies using dual meteor detections from these two radars, focusing on finding the meteor mass using the radar cross section of both radars. One of the main aspects in this thesis is also to find the radar cross section for the different meteor observations for both radars, but in this work, the radar cross section is used to identify what kind of ablation and fragmentation the meteor undergoes.

This work utilizes different signatures in the data from both radars to characterize different types of ablation events and fragmentation events (Malhotra and Mathews, 2011). The second of two main goals in this thesis is to use these signatures in the data from both EISCAT UHF and MAARSY to examine the occurrence rates of the different processes. Case studies of individual meteors are also conducted to more closely examine the signatures and their associated processes.

The first main goal in this thesis is to investigate the range timing for the EISCAT UHF radar data. Due to the signal being recorded in a control building, not directly at the radar dish, some corrections may be needed for the range measurements performed by the radar. An offset in the range measured by EISCAT UHF could cause a discrepancy when comparing results from EISCAT UHF and MAARSY. It is therefore important to find and apply this offset before performing any analysis of meteor events using both radars to achieve the second main goal of this thesis.

This thesis begins by introducing necessary theory for the processes undergone by meteors in the atmosphere as well as radar theory in Chapter 2. Chapter 3 goes into further detail about the two specific radars used in this work. Chapter 4 presents the method for and results of investigating the timing of the EISCAT UHF radar. Chapter 5 explains the methods used in the meteor study work of the thesis, for each of the radars individually and also for using both radars simultaneously. The data analysis and discussion of results are presented in Chapter 7. Finally, a summary of the thesis is given in Chapter 8.

2

Background

In this chapter, the theory used to classify different atmospheric processes through radar data is presented. Section 2.1 introduces what the meteors that enters our atmosphere are and where they originate from through the introduction of cosmic dust. The processes the meteors undergo as they travel through Earth's atmosphere are explained in Section 2.2. Section 2.3 discusses how these meteors and processes can be observed through the use of radar technology.

2.1 Cosmic dust

Cosmic dust is a collection of icy, heat resistant particles in the solar system ranging in size from only a few micrometers to around a meter (Koschny et al., 2019). The mass injection into the atmosphere that occurs from cosmic dust entering the atmosphere has been researched and estimated for decades. Several techniques exist for measuring mass injection, each spanning different mass ranges. Together, these techniques yield a large range of measurable mass injection. This mass injection is important for several reasons. An accurate estimate of the mass that enters the atmosphere can be used to confirm the dust evolution in the solar system and how the dust is transported from the middle atmosphere to the Earth's surface, thereby giving a better understanding of the processes undergone by the cosmic dust in the Earth's atmosphere. The estimate of cosmic dust reaching the surface of Earth could, together with the

estimate of cosmic dust entering in the atmosphere, explain these processes. Without an accurate mass estimate, there is uncertainty in our understanding around the velocity of the vertical transport of dust in the middle atmosphere and how the dust is transported from the middle atmosphere to the surface of Earth (Plane, 2012).

The cosmic dust that travels in the inner solar system consists of comets, asteroids and meteoroids. The difference between comets and asteroids is their composition: they are both made of rocky materials, but comets are icy and asteroids are metallic. Meteoroids are small asteroids that can be as small as a few dust grains of 10^{-4} μg or as large as 100 g (Limonta et al., 2020). These objects are called meteoroids when they are travelling in space, but when they enter the atmosphere of Earth they are called meteors. If the meteor lands on the surface of Earth after surviving its entry through the atmosphere, it is called a meteorite (NASA.gov, b).

The cosmic dust that enters the atmosphere of Earth undergoes processes explained later in this section. The result of these processes is that particles from the cosmic dust will be injected into the atmosphere. These particles are metallic and will form layers of metal atoms and ions, which will in turn impact the O_3 chemistry in the atmosphere, be involved in the formation of noctilucent clouds and play a role in several other phenomena that can, for instance, be used as a measure of climate change (Plane, 2012).

Cosmic dust that is found in the inner solar system has four main known sources: Jupiter Family comets, Halley Type comets, Oort Cloud comets and asteroids (Garrillo-Sánchez et al., 2016). Of these four, the main source is the Jupiter Family comets. These are short-period comets contributing to about 80% of the total mass input to the atmosphere. This value is found by observing the Na and Fe fluxes above 87.5 km altitude with a lidar and comparing the results to a model of the cosmic dust from all four sources. This result is also supported by measurements of the accretion rate of cosmic spherules, small micrometer-sized particles that accumulate over time, performed at the South Pole (Garrillo-Sánchez et al., 2016).

Cosmic dust is input into the inner solar system from these sources due to collisions between asteroids or sublimation of comets when they move closer to the sun. Comets crossing the orbit of Earth lead to meteor showers by leaving behind dust. This dust enters the atmosphere as Earth passes through it. This is the origin of the Geminids meteor shower caused by asteroid 3200 Phaethon, which is analysed in this work (NASA.gov, a). However, meteor showers caused by comets or asteroids crossing Earth's orbit are not the only source of meteor particles entering the atmosphere. Sporadic meteors, which are meteors that cannot be associated with a known meteor shower, are the source of the largest

mass flux. They come from long-decayed cometary trails and the asteroid belt (Plane, 2012). This continuous flux of sporadic meteors can also be seen during meteor showers, as will be seen in the radar data analysis in Chapter 6.

2.2 Atmospheric processes

As a meteor enters the atmosphere it undergoes different processes. The velocity of the meteoroid can be anywhere from 12 to 72 km/s (Limonta et al., 2020). The processes acting on the meteor are a function of its velocity and mass and thus can vary wildly from meteor to meteor (Limonta et al., 2020). Meteors experience ablation in the form of rapid heating, vaporization, and erosion due to friction generated by atmospheric drag. Most of the meteors entering the atmosphere ablate completely and do not make it down to Earth's surface. The meteors can experience simple ablation, differential ablation and fragmentation as they move through the atmosphere, which are the processes this thesis is focusing on (Malhotra and Mathews, 2011).

The meteor undergoes ablation because the aerodynamic pressure in the atmosphere is greater than the strength of the material composing the meteor. This pressure will generate heat and cause the meteor to break apart. The ablation rates are determined by the speed and composition of the meteor.

2.2.1 Ablation

If the meteor has a homogeneous composition, it will experience ablation at a constant rate, called simple ablation. The meteor can also experience simple ablation if its constituents have similarly high heat resistances. When the meteor moves through the atmosphere it will gradually experience a higher temperature due to a higher aerodynamic pressure. If the meteor consists of only particles with a high heat resistance, like Mg, Fe and Si seen in Figure 2.1, it will not experience a sudden ablation.

However, if the meteor consists of materials with different heat resistances, the meteor will experience differential ablation. In differential ablation, the most heat-resistant particles, such as Ca, Fe and Si, are still present in the meteor while less-heat resistant particles, such as Na and K, completely ablate, which can be seen in Figure 2.1. This differential ablation results in a sudden mass loss, unlike the continuous mass loss that simple ablation yields (Malhotra and Mathews, 2011). This sudden mass loss will occur at an altitude of around 100 km, according to Figure 2.1.

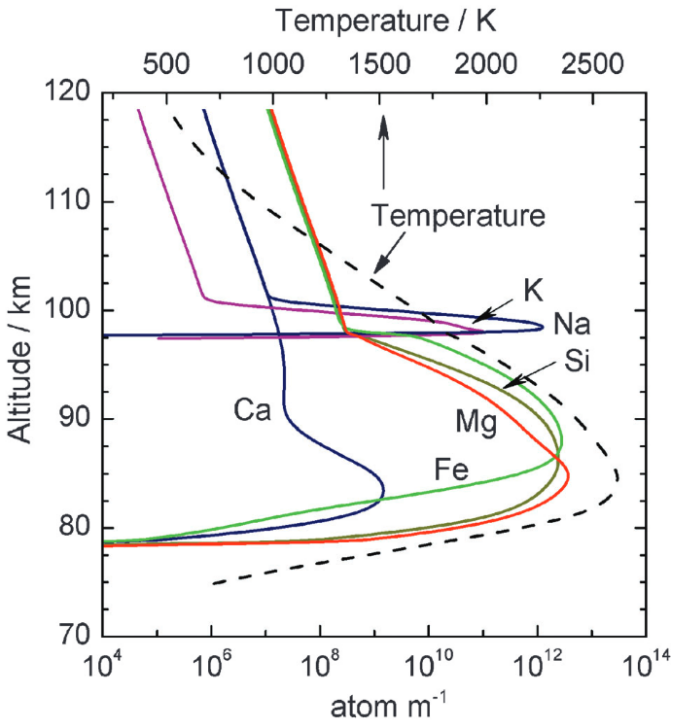

Figure 2.1: Ablation profiles for a 5 μg meteoroid entering the atmosphere at 20 km/s, predicted by the Chemical Ablation Model (CABMOD). Illustration taken from (Plane, 2012).

2.2.2 Fragmentation

If the meteor breaks apart into smaller pieces which are not vaporized or eroded but remain as two or more separate objects, the process is called fragmentation. These pieces break apart due to the pressure exerted on the meteor by atmospheric forces. Shortly after they break apart, they will move together along nearly the same trajectory because they originate from the same parent body. In some cases, the process causing them to break apart can result in the initial velocity of one of the pieces to be higher than the other. After some time, they move further and further away from each other. The more different the pieces' acceleration is, the faster they start moving away from each other. Depending on the size of the meteor fragments and the distance between them, they can each be seen as individual meteors (Malhotra and Mathews, 2011).

2.2.3 Meteor plasma

Regardless of which ablation process the meteor undergoes, its outer layers will be converted to a plasma. This is due to sputtering, particles ejected from a solid surface after bombardment by energetic particles, and frictional heating that happens as the meteor moves through the atmosphere. This ablation and formation of plasma happens when the meteor has an altitude between 80 and 120 km, depending on its size, composition and velocity. The plasma that is surrounding the meteor is called the head plasma and moves with the meteor. As the meteor continues on its trajectory, some plasma gets left behind, called the meteor trail (Tarnecki et al., 2021).

Radars are capable of receiving echoes from both the meteor trail and the head echo plasma. The meteor trail can be further classified into specular or non-specular, depending on how the radar waves are backscattered. In nonspecular trails, the radar signal is scattered differently due to plasma turbulence originating from plasma density waves developing on the edge of the trails, while specular trails are the quasi-stationary extended plasma left behind the meteor (Close et al., 2002). This thesis focuses on the meteor head echoes.

More accurate explanations for the scattering mechanism causing this head echo have been developed in the last few years. One of the newest models is the Finite Difference Time Domain (FDTD) model developed by Marshall and Close (2015), modelling the scattering of radar signals from meteor head plasma (Marshall and Close, 2015). Previous models have assumed that the head plasma distribution is spherical and given by a Gaussian curve. These simplified models have yielded results that do not match reality. In these models it has also been assumed that the meteor scatters like a conducting sphere. The size of this conducting sphere is determined by the region where the plasma frequency exceeds the radar signal frequency, called the overdense region (Close et al., 2002). Depending on the radar frequency and the electron density of the meteor plasma, the overdense region is of different sizes. This region can more easily be detected by lower frequency radars. Some meteors can have both overdense and underdense regions, depending on the radar frequencies that are observing the meteor (Marshall and Close, 2015).

The FDTD model does not make these assumptions but instead solves Maxwell's equations and the Langevin equation in and around the plasma. This allows for a relation between the radar cross section (RCS) and parameters such as plasma densities, meteor scale sizes and radar frequencies (Marshall and Close, 2015). Using this model, they have shown results that suggest meteor head echoes may also be detected in the underdense region, where the plasma frequency is comparable to or less than the radar wave frequency. The RCS and its relationship with the radar frequency is described further in the following

section.

2.3 Meteor measurements

There are many techniques to gather information about meteors, including analysing craters on satellites, using optical meteor cameras, Zodiacal dust cloud observation and theoretical modeling (Plane, 2012). Figure 2.2 shows some of these techniques together with the meteor mass range they cover. The "huge impactors" seen in Figure 2.2 contribute to a large mass influx, but are rare events and will not be considered here.

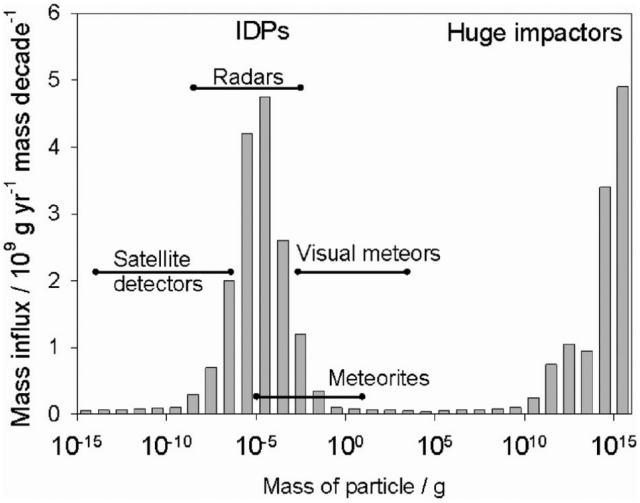

Figure 2.2: Representation of different meteor observation techniques together with the mass ranges they cover. Illustration taken from (Plane, 2012).

Figure 2.2 shows that radars cover the largest mass range and largest mass influx, and are therefore a widely used technique. High Power Large Aperture (HPLA) radars can be used to measure the plasma forming around the meteor. The radar can not directly measure the meteor, but instead measures the RCS for the meteor head echo plasma. RCS is a measure of how detectable a target is to the radar. The larger the RCS a target has, the more easily the radar can detect it. The RCS depends on many factors, including the size, shape, composition, velocity, altitude and orientation of the target and also the radar frequency. The peak RCS of meteor head echoes is calculated to be at around 100 km altitude (Tarnecki et al., 2021).

Radars can be used to observe meteors entering the atmosphere. The time

between the transmission of a signal from the radar and the reception of an echo with power higher than a determined noise level is recorded. This time determines the range to the object that the echo originated from.

The radar frequency is an important factor in determining the RCS of an object that is measured. The equation for determining the RCS can be derived from the radar range equation, which is given as (Murad and Williams, 2002)

$$P_r = \frac{P_t G_r G_t \lambda^2 \sigma}{(4\pi)^3 R^4} \tag{2.1}$$

where P_r is the received power, P_t is the transmitted power, G_r is the receiver antenna gain, G_t is the transmitter antenna gain, λ is the radar wavelength, σ is the radar cross section, and R is the range from the radar to the target. Due to the use of monostatic radars, G_t and G_r will be treated as the same gain, G, for the remainder of this work.

The RCS can be expressed from equation 2.1 giving:

$$\sigma = \frac{(4\pi)^3 R^4 P_r}{G^2 \lambda^2 P_t}. \tag{2.2}$$

By assuming overdense reflection, the electron density as a function of distance away from the meteor center can be illustrated as in Figure 2.3.

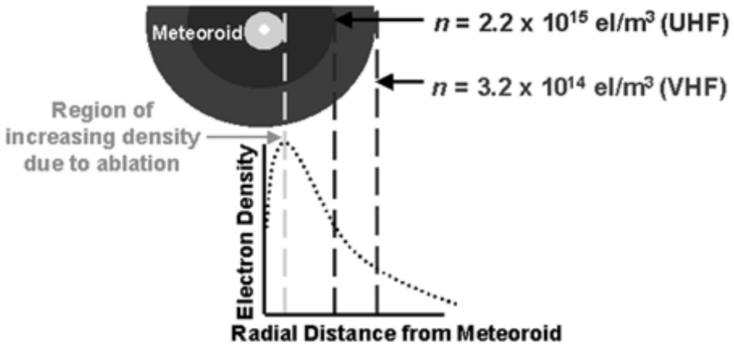

Figure 2.3: Electron density varies as function of distance from meteor center. This is a theoretical illustration, to show how the density varies and how this determines at which distance the radar signal gets backscattered. Illustration taken from (Close et al., 2002).

The plasma frequency can be given as $f_p = 9000\sqrt{n}$ and would therefore be

greater as the electron density, n, increases (Close et al., 2002). A radar wave from an Ultra High Frequency (UHF) radar would have to penetrate deep into the meteor plasma region to reach the boundary where the wave is scattered, when assuming overdense reflection, because of the increasing electron density. For a Very High Frequency (VHF) radar (with a lower frequency than UHF), the radar wave is backscattered at a lower electron density (Close et al., 2002). This implies that radars with lower frequencies have higher RCS than radars with higher frequency, as the meteor plasma region appears larger.

2.3.1 Radar observations

When a radar is used to measure a meteor, the signal to noise ratio (SNR), which is a measure of the strength of the received signal, can be used to analyse which types of processes the meteor has undergone both before and during the radar detection. The pulse integrated SNR, called a light curve by Malhotra and Mathews (2011), is used in determining these processes.

Simple ablation

Simple ablation is ablation at a constant rate, as explained in Section 2.2.1. When ablation happens at a constant rate, the light curve will follow the radar beam pattern for the radar used in the measurement, and therefore be a smooth curve (Malhotra and Mathews, 2011).

Figure 2.4 shows an example of a light curve representation of a meteor event undergoing simple ablation. The light curve is defined as a pulse-integrated SNR over the total time of the meteor event (Malhotra and Mathews, 2011). This light curve will be referred to as the SNR for the meteor event throughout the rest of this thesis.

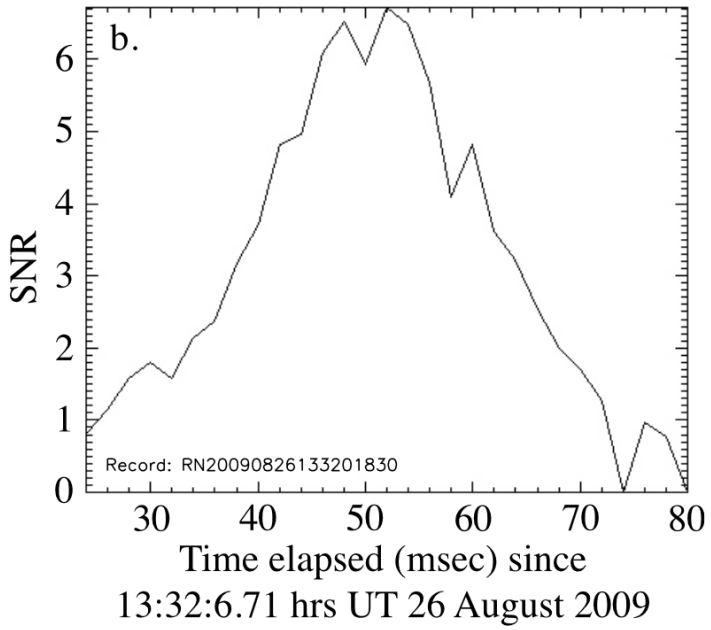

Figure 2.4: Example of a meteor event experiencing simple ablation showed through the SNR as a function of time. Illustration taken from Malhotra and Mathews (2011).

Figure 2.4 shows a relatively smooth SNR following the radar beam pattern. In this case, the radar beam pattern can be seen as approximately a simple Gaussian.

The RCS can also be used to determine what kind of processes the meteor is experiencing, as it is a measure of how detectable the meteor is to the radar. If the meteor does not suddenly change composition or shape, the RCS would be expected to stay constant or slowly decay over time. This is connected to the smooth SNR seen in Figure 2.4.

Differential ablation

Due to the sudden mass loss that is the result of differential ablation, a clear drop is expected in both the SNR and the RCS (Malhotra and Mathews, 2011). Figure 2.5 shows the SNR curve for a meteor event experiencing differential ablation.

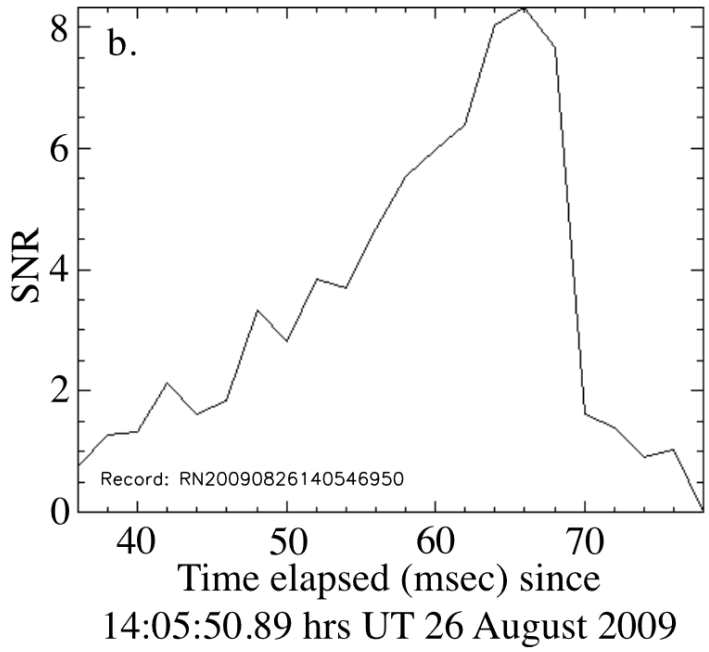

Figure 2.5: Example of a meteor event experiencing differential ablation showed through the SNR as a function of time. Illustration taken from Malhotra and Mathews (2011).

A clear drop in the SNR, seen in Figure 2.5, indicates that the meteor is experiencing a sudden mass loss and hence differential ablation. If differential ablation is the only process the meteor is undergoing, a smooth SNR curve is expected both before and shortly after the drop.

A clear drop can also be seen in the RCS for the radar during a differential ablation event. The RCS value is expected to stay at the level it reached after the drop, as the meteor has lost constituent particles and is now more difficult for the radar to detect.

Fragmentation

When the meteor breaks into two or more fragments, the SNR curve is expected to show a beat pattern. When the fragments break apart, and shortly after, they move together with slightly different velocities because they are of different masses and shapes. Since they originate from the same meteor, they will begin close to each other and progressively move further and further away from the original body and other fragments (Malhotra and Mathews, 2011).

Figure 2.6 shows one example of this beat pattern in the SNR that is associated with meteor fragmentation.

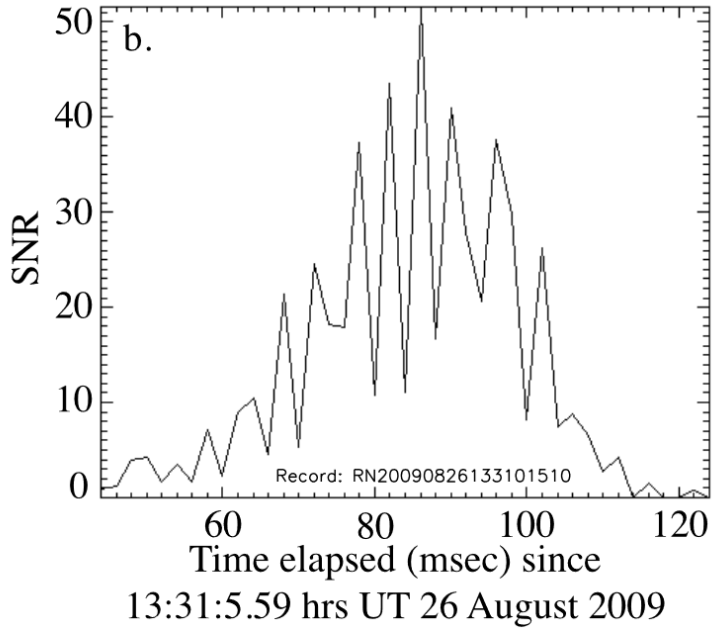

Figure 2.6: Example of a meteor event experiencing fragmentation showed through the SNR as a function of time. Illustration taken from Malhotra and Mathews (2011).

This beat pattern seen in Figure 2.6 in the SNR is also expected to be seen in the RCS. The beat pattern observation arises from the fragments decelerating at different rates, therefore changing the distance between them. When the fragments are measured by the radar at the same time, the two scattered waves will have different phases once they are received by the radar, depending on the distance between the fragments. If an odd multiple of the radar wavelength separates the fragments, the received signal will be out of phase and destructively interfere. But, as the fragments move further apart, there will be detections where an even multiple of the radar wavelength separates the fragments and they will be in phase, constructively interfering (Kero et al., 2008a). This in-phase and out-of-phase scattering is the reason for the beat pattern occurring in the SNR and hence also in the RCS that is seen in Figure 2.6 (Malhotra and Mathews, 2011).

3

Radars

3.1 EISCAT UHF

The European Incoherent SCATter (EISCAT) is a scientific organization that conducts atmospheric and ionospheric measurements with radar. There are EISCAT radar sites in Ramfjordmoen (Norway), Kiruna (Sweden), Sodankylä (Finland), and Svalbard (Norway). This work uses data from the 32 meter EISCAT Ultra High Frequency (UHF) radar located in Ramfjordmoen outside Tromsø, at 69°35′N 19°14′E (EISCAT.se). The UHF radar is a monostatic radar, meaning that it receives and transmits using the same antenna.

During the campaigns used in this work, the radar was transmitting at a frequency of 930 MHz using the manda experiment. The experiment contains instructions to the radar ensuring that transmitting, receiving and signal processing are performed properly and at the specific times needed to measure the desired ranges. The manda experiment is optimized for the range span 19-209 km, but will continue to receive signal from further ranges. The manda experiment has a time resolution of 4.8 s using the EISCAT UHF supported GUISDAP software package. The EISCAT UHF radar has a sampling rate of 1.2 μs and a transmit code with a baud rate of 2.4 μs. Each pulse uses a different 61-bit code. Because the radar is monostatic, it is unable to receive while it is transmitting. As a result, some ranges will not be detected by the radar. The range measured by the radar can be found with the formula

$$\Delta t = \frac{2r}{c} \rightarrow r = \frac{c\Delta t}{2} \tag{3.1}$$

where Δt is the signal travel time, c is the speed of light (299,792,458 m/s) and r is the range.

The EISCAT UHF radar with the manda experiment has a pulse length of 146.4 μs (61-bit x 2.4 μs) and an inter pulse period of 1500 μs. The transmitting starts at 73.6 μs while the receiving starts at 343 μs and ends at 1473 μs. This information allows the calculation of which ranges the radar is transmitting and receiving. Figure 3.1 shows the approximate ranges where the radar is receiving and transmitting found using equation 3.1.

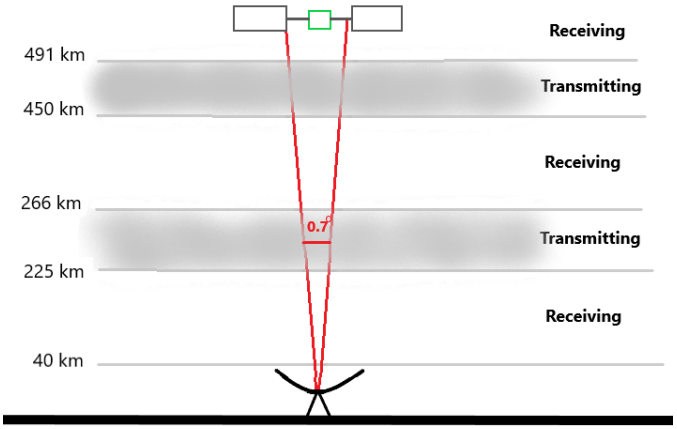

Figure 3.1: Illustration of at which ranges the radar transmit and receives. No part of the figure is to scale. The figure is just for illustration purposes. The half power beam width value of 0.7 deg is taken from Schult et al. (2021). Illustration taken from project paper work.

This work uses two EISCAT UHF datasets. The first dataset, from the 2022 Geminids meteor shower, is used to calibrate the radar. The second dataset, from the 2023 Geminids meteor shower, is used for meteor detection and analysis. During the 2022 Geminids meteor shower campaign the EISCAT UHF radar was run continuously from 12.12.2022 at 12:00 UTC until 15.12.2022 12:00 UTC. During the 2023 Geminids shower, between the dates 06.12.2023 and 13.12.2023 the radar was run from 00:00 UTC until 06:00 UTC, while it was run continuously from 00:00 UTC 14.12.2023 until 23:59 UTC 15.12.2023. The manda experiment was used for both campaigns, meaning both have the same experiment parameters. The only difference between the campaigns is the pointing direction. The 2022 campaign had the radar pointed at zenith, while the 2023 campaign had the radar pointed above the MAARSY radar. The field-of-views of the two radars overlapped at approximately 100 km altitude. The first part of the processing of

both datasets utilizes the same meteor processing code, with some adjustments to cover the desired range for the calibration part of the project. This processing is described in Section 4.1.

Azimuth and elevation are, together with range, used to determine the location of a detected echo. Azimuth is the angle of the radar with respect to north, so it contains information about which direction the radar is facing. Elevation is the angle the radar is pointing over the ground plane, so it contains information about how high the radar is pointing (celestis.com). For the 2022 Geminids, the EISCAT UHF radar was pointing at zenith, meaning directly upward to the sky. For the 2023 Geminids, the radar was pointing with an azimuth of 257.1° clockwise from north and an elevation of 37°.

The beam pattern, or the radiation pattern, of a radar describes the intensity of energy radiation as a function of the angle from boresight, which is the center of the beam. The EISCAT UHF beam pattern is shown in Figure 3.2, obtained empirically from previous experimental measurements, and is considered accurate. The beam pattern is rotationally symmetric about the center axis of the beam. The EISCAT UHF gain for a given an angle from boresight can be found from this beam pattern.

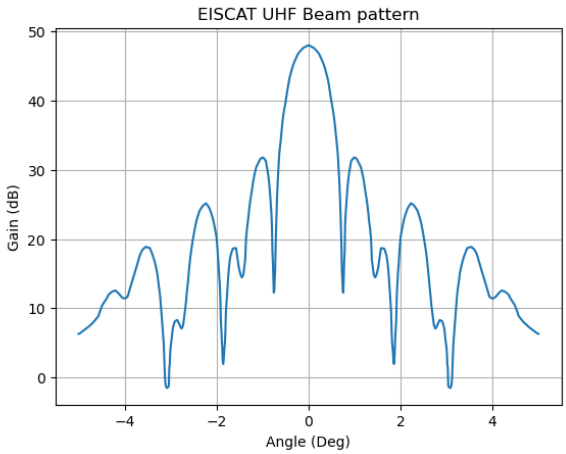

Figure 3.2: EISCAT UHF beam pattern. Obtained from measurements by Juha Vierinen.

The mainlobe is the center part of Figure 3.2, from 0° to about 0.7°. This mainlobe approximately follows a Gaussian function. This is not the case for the sidelobes, seen in Figure 3.2 as the lobes at angles greater than 0.7°. The subreflector on the EISCAT UHF radar is large compared to the radar diameter which causes this beam pattern shape.

3.2 MAARSY

The Middle Atmosphere ALOMAR Radar System (MAARSY) is a monostatic radar located at 69.30°N, 16.04°E in Andøya, Norway. MAARSY is a phased array radar where 433 Yagi antennas operate together. Because of this, the radar has flexible beam steering and beam forming making interferometric applications possible. The radar operates at 53.5 MHz and has a minimum half power beam width of 3.6°. The antenna is organized in a way so that the overall array is a circular shape, through dividing the array into a total of 61 subgroups. The interferometric applications allow the accurate determination of the position of the detected meteor echoes (Latteck et al., 2012).

4

Calibration work

In this chapter, the calibration part of the thesis is explained and the results presented. Section 4.1 explains the method used for this calibration, which was initially developed during the project paper work, including both how the TLEs for the satellites are found and how the same satellites are found in the EISCAT UHF radar data. The results and conclusion of this work are presented in Section 4.2.

4.1 Calibration method

Several previous measurements and experiments have shown unexplained differences between EISCAT UHF measurements and measurements from other radars despite the simultaneous measurements of the same object (Schult et al., 2021) (Tarnecki et al., 2021) (Close et al., 2002). For this reason the range timing of the EISCAT UHF radar system must be verified and calibrated if needed.

A radar determines the range to the measured object or phenomena by recording the time between transmission of the signal from the transmitter location and reception of the reflected signal at the receiver location. This time can then be converted into a distance using equation 3.1. The EISCAT UHF operating facilities are located close to the radar. The time and hence the range are recorded from the operating facilities, not directly from the radar location.

It is therefore thought that this range does not reflect the true range from the radar and to the object, but also includes delays from the signal feedlines and/or waveguides to the radar control building. This will increase the range to a target in the analysis of EISCAT UHF measurements, and could explain some of the differences between EISCAT UHF and other radars when doing the same measurements. An investigation into whether the EISCAT UHF data has a time/range lag will give results that can be applied to further calculations using EISCAT UHF data and could reduce some of the differences between EISCAT UHF measurements and measurements from other radars, including MAARSY.

The process of calibrating the EISCAT UHF radar uses satellites observed by the radar during the 2022 Geminids meteor shower campaign. Two Line Elements (TLEs) are found for these satellites, which give a position estimate for the time period the satellite is observed. This position will be compared with the range found by the radar. This method is explained in sections 4.1.1 and 4.1.2.

The work for calibrating the radar was started as a project paper during the fall of 2023. To ensure reliable results that could be used in further work, the work with the calibration was continued from the project paper into this master's thesis. Therefore, descriptions of the method and the theory behind this work contain parts similar to the project paper as this is a further investigation of the same work using a similar method and the same dataset.

4.1.1 Satellite Two Line Elements

The idea behind the calibration of the EISCAT UHF radar is to examine satellites detected by the radar during the Geminids meteor shower campaign in 2022. The ranges of these satellites given by the radar measurements can be compared to ranges found using the TLEs of the satellites. Comparing these two ranges will give an estimate of the range offset of the radar. This offset can then be applied to further radar analysis to give a more accurate result.

The first step was to find TLEs for satellites that could have been detected by the radar. Each satellite and space junk object orbiting the Earth has a TLE describing the orbit of the object. They contain relevant information about the satellite for a given epoch time. The epoch time for a TLE specifies the moment in time at which the orbital parameters in the TLE are valid. The epoch is therefore the starting point from which the orbital motion of the satellite is predicted. The further from the epoch time the TLE is used, the more inaccurate it becomes. Normally a satellite will receive an updated TLE every 2-5 days, depending on its orbit, how many perturbations it experiences from the atmosphere, and how old the satellite is, as this will influence its

stability.

The time of theoretical closest approach of the satellite to the radar site and the satellite altitude can both be derived from the TLE and are necessary to perform the calibration. This is further explained in Section 4.1.2. For this reason, the satellite TLEs were found first. The satellites were found by the use of space-track.org, which is a website promoting space flight safety and sharing space situational awareness services. The website is managed by the 18th Space Control Squadron, a United States Space Force Space Domain Awareness unit (18th Space Control Squadron). Space-track.org contains a Query Builder function that creates json files consisting of TLEs. Requirements for the TLEs, such as the time period of their epoch time and inclination value, are given to the Query Builder function to narrow down the number of TLEs. The requirements shown in Figure 4.1 were used in this work as they were found to include a large number of satellites that were possible candidates to be detected by the radar.

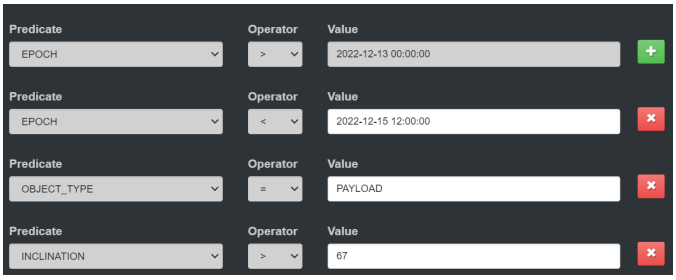

Figure 4.1: Settings on space-track.org creating TLEs in the desired time period (18th Space Control Squadron).

The epoch time interval is decided by the time period of the radar campaign where the radar data used in this work originates from. This ensures that TLEs from satellites seen in the radar data are included in the json file generated by space-track.org. Since the website also tracks space debris, the object type is defined as payload to ensure that only satellites get included. The higher the inclination of the satellite orbit, the higher latitudes it covers. An inclination of 90° orbits around the poles. The EISCAT Ramfjordmoen facility has a latitude of 69° and the inclination given to the Query Builder is based on this, but as a lower estimate to include every possible satellite.

From the orbital elements derived from the individual TLEs, the satellite trajectories were found by using the Skyfield package for Python (rhodesmill.org). This package contains an EarthSatellite object which takes in the TLE for the satellites and then can be used to find the geographic positions of the orbit corresponding to the TLE. As the TLE is hard to understand itself, this tool was

used to easily obtain access to orbital information. The altitude of the satellites can be found directly from the EarthSatellite object.

For each individual satellite, the orbit over a period of 24 hours is divided into points approximately one second apart. The radar site is located at a high latitude and the satellites that are passing over are in near-polar orbits, with a period of around 90 minutes (Low Earth Orbit). The epoch time which the satellite TLE is collected from is not necessarily the time the satellite passes over the radar, as the epoch time represents the start time of the TLE. Therefore, a period of 24 hours is chosen. In this time the polar orbit satellites will have orbited the Earth multiple times which increases the chance of finding the specific satellite pass that is detected by the radar.

For each approximately 1 second point in the 24 hour time interval, the longitude and latitude of the satellite are found from the EarthSatellite object. These coordinates are compared to the coordinates of the EISCAT UHF radar site ± 0.2 degrees for both latitude and longitude. Every latitude and longitude point is looped through and checked as a pair and if both latitude and longitude coordinates for the satellite, determined from the TLE, are within the respective EISCAT UHF coordinate range, the satellite object is saved. The time of closest approach is also saved to increase the chance of finding the satellite in the radar data later in the process.

The point of closest approach requires calculating the distance between the satellite and the radar. These distances are found by transforming the latitude, longitude and altitude coordinates of both the satellite and the radar to geocentric coordinates and calculating the 3-dimensional distance between them.

4.1.2 Radar data

The time of the closest distance between the satellite and the radar site is used to determine which radar files to analyse for satellites. The distance calculated between the satellite and radar is also used to limit the number of ranges that are evaluated in the radar data analysis.

The radar experiment and code used to analyse the data is similar to that used in the project paper. The description below is therefore similar to the description provided in the project paper.

Using the manda experiment on the EISCAT UHF radar, raw complex voltage data is the basic data output. A conversion script is used to convert the raw complex voltage data to the DigitalRF format for ease of use (MITHaystack).

Both the transmitted and received signal are saved in Hierarchical Data Format (HDF5) files and used in the analysis. The starting point for this analysis is previously developed software for detecting meteor head echoes. This software is modified to be used for detecting satellites, although the base of it is the same.

The transmitted signal is saved in directories on a server, each directory containing one hour of runtime on the radar with files for every 4.8 seconds. Each of these files again contains 25 coded pulse sequences made up of 128 coded pulses each. Each coded pulse is analyzed individually, and the timing between each pulse is 1.5 ms. The time between possible detection points is therefore 1.5 ms. To avoid looking through all these files for the entire campaign period, the time of the closest distance (as described in Section 4.1.1) is used. In this way only the times the satellite passes over the radar site are considered.

To further reduce the quantity of data to be analysed, the distance between the satellite and the radar at the time of the closest distance is used. It is expected that the distance found by the radar differs from the distance found by using the TLE, but this difference is not expected to be large compared to the total range measured by the radar. To find the time at which to start receiver data analysis, a time offset is calculated using equation 4.1 and added to the start receiver time.

$$\Delta t = \frac{2r}{c} \tag{4.1}$$

where r is the distance calculated using the TLE and c is the speed of light. The transmitted files, which are decided from the closest time found in Section 4.1.1, and the offset, determined by the distance from the radar to the satellite, determines the start index of the first received sample. This first received sample gets analysed based on the transmit pulse that most closely matches the timing.

To analyse the radar data, this method decodes the received signal by taking advantage of the fact that the transmitted waveform is known. A matched filter is a signal processing filter that utilizes this. The filter cross-correlates the received signal with a reference signal, which in this case is a time-reversed and complex conjugate version of the transmitted waveform. This will amplify the components in the received signal that match with the transmitted signal and suppress the components that differ. The signal-to-noise ratio (SNR) will be maximized by minimizing the noise and interference in the received signal (Richards, 2014).

For measuring the similarity between two signals, cross-correlation can be used. This will then show a peak in amplitude where the two signals are similar. The cross-correlation for a continuous time series is given by (Richards, 2014)

$$(x \cdot y)(\tau) = \int_{-\infty}^{+\infty} x(t) \cdot y(t+\tau) dt. \tag{4.2}$$

The idea with the matched filter is to correlate the received signal with a known reference signal. By maximising the correlation between the received signal and the reference signal, the presence of the desired signal can be detected even when noise is present. The matched filter output is given by the convolution of the received signal and the time-reversed conjugate of the reference signal. For this, a time series for each range is created by:

$$y(t, r) = x(t) \cdot s^*(t - \tau) d\tau \tag{4.3}$$

where $x(\tau)$ is the received signal and $s^*(t - \tau)$ is the complex conjugate of the time reversed reference signal (Richards, 2014). τ is proportional to the range, r.

A Fourier transform is taken on each $y(t, r)$. This gives a frequency domain representation of the received signal. The discrete Fourier Transform is defined as

$$\hat{x}[k] = \mathcal{F}_D x[n] = \sum_{n=0}^{N-1} x[n] e^{-i\frac{2\pi}{N}nk} \tag{4.4}$$

where $x[n]$ is a periodic discrete-time signal, N is the period of $x[n]$ and k is an arbitrary integer (Vierinen, 2021).

To calculate the Fourier transform for a real dataset, the Fast Fourier Transform (FFT) algorithm is much faster. The algorithm calculates the Fourier transform by subdividing it into shorter Fourier transforms (Vierinen, 2021). Python provides a FFT package that is used in this work. The FFT is taken on each $y(t, r)$ so that a range-Doppler spectra is obtained as $y(f, r)$. The zero-frequency is shifted to the center of the spectrum using the same FFT package. To analyse the range-Doppler power from this Fourier transform, its absolute value is squared.

The next step is to detect if a desired signal is present. This is done by introducing a noise floor and if the value of the signal after the Fourier transformation exceeds this noise floor it indicates that the desired signal is present. This desired signal is then the transmitted signal that is reflected back to the radar from some type of object in the radar field-of-view. The median absolute deviation (MAD) is used to find this noise floor estimate. MAD is found from the signal as the average distance between each point and the mean of the total signal, defined as (Rousseeuw and Croux, 1993)

$$MAD = b \cdot M_i(|x_i - M_j(x_j)|) \tag{4.5}$$

where $M_i(|x_i - M_j(x_j)|)$ represents the median of the signal and b = 1/0.67449 = 1.4826 and is a constant linked to the assumption of normality in the data set (Rousseeuw and Croux, 1993).

To find the parts of the received signal that exceed this noise floor, the signal-to-noise ratio is defined with the following equation:

$$SNR = \frac{\text{FFT(signal)} - \text{MAD}}{\text{MAD}} \tag{4.6}$$

where FFT(signal) is the Fast Fourier Transform of the radar signal and MAD is the noise floor estimated from equation 4.5.

For each pulse, if the max SNR is greater than an empirically determined threshold, the SNR value, the Doppler and the range for that pulse are saved and it is assumed that this signal is from an object, like a meteor or a satellite.

Interpolation for these specific ranges in the radar data is then performed. This is to get more detailed information about the signal in this analysis, as interpolation estimates unknown values between the known values. The signal is sampled at double the transmit code rate, and the target can be considered small in the range gate. The FFT resolution is also increased to obtain a more accurate estimate of the Doppler shift of the object, which works when assuming that the small target moves at a relatively constant velocity during the pulse. This is not done at an earlier stage in the analysis to avoid performing interpolation on data without any interesting aspects. Doing the interpolation after finding SNR above some threshold reduces the amount of data being interpolated.

The received and transmitted samples are interpolated in time with an interpolation factor of 20. The range-Doppler values for the interpolation values are

calculated in a similar way as the original samples.

The radar pulses containing a high peak in the SNR in the time interval that corresponds to the times that satellites are overhead (according to their TLE) are compared individually. The satellite range detected by the radar after interpolation is compared to the satellite range calculated from the TLE for each satellite found in the radar data. The differences between these ranges are found and will be a measure of the range offset of the radar.

4.2 Calibration Results

The original file with satellite TLEs that was made by using the requirements from Figure 4.1 contained 24912 satellites. After applying an altitude upper limit of 750 km, because this is the maximum range analysed in the radar data, 14706 satellites were included in the further calculations.

47 satellites were found to have an orbit that passed over the radar site in the time period during the radar campaign. These can be seen in Table A.1 in Appendix B. Out of these, 13 were found in the radar data. These 13 are presented in Table 4.1 sorted according to their epoch time from TLE. The time presented in the table is not the epoch time, but the time the satellite was closest to the radar site. The average radar range is the average of the interpolated range found from the radar analysis while the average TLE range is the average satellite altitude found by using TLEs. The approximate difference between these ranges is found by averaging the difference for each point in the satellite's orbit.

Table 4.1: Satellites detected by the EISCAT UHF radar. The satellites are sorted by their TLE epoch, not the time of closest approach, which is displayed here.

Satellite	Time (UTC)	Radar rng (km)	TLE rng (km)	Diff (km)
STARLINK-3095	13.12 02:38:48	586.5704	585.2138	1.35669
STARLINK-3057	13.12 21:53:36	586.6280	585.4412	1.18384
ONEWEB-0595	13.12 15:02:24	607.8167	606.8806	0.93605
STARLINK-3077	14.12 00:27:36	587.0275	586.0723	1.08527
OSCAR 11	14.12 04:27:00	622.9558	622.1165	0.83922
KHALIFASAT	13.12 14:20:00	607.1901	606.3467	0.84343
STARLINK-4334	14.12 06:54:12	574.5798	573.9475	0.62436
STARLINK-4347	14.12 17:43:24	575.8004	574.9112	0.88914
DUMMY MASS 2	14.12 17:48:36	620.5215	619.6899	0.83832
ICUBE 1	15.12 05:25:24	600.0833	599.2075	0.87577
STARLINK-3078	15.12 02:01:24	586.9232	585.8283	1.09293
STARLINK-3077	15.12 00:30:00	587.1714	586.0723	1.06512
STARLINK-3085	14.12 23:27:24	586.6543	585.2570	1.39736

The orbit tracks for the satellites in Table 4.1 are shown in two different views in Figure 4.2 and Figure 4.3. The orbits are plotted for the time the satellite was closest to the radar site, as seen in Table 4.1. This figure shows that all these orbits are over the radar site, which is the red dot that can barely be seen at the point where all the orbits cross over.

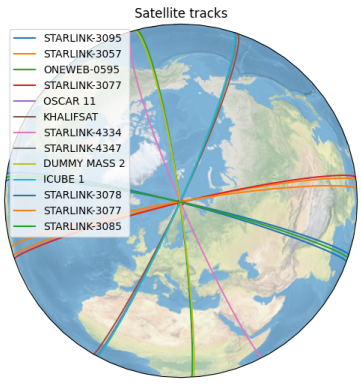

Figure 4.2: Satellite tracks for the satellites found in the radar data plotted over the time when they are closest to the radar.

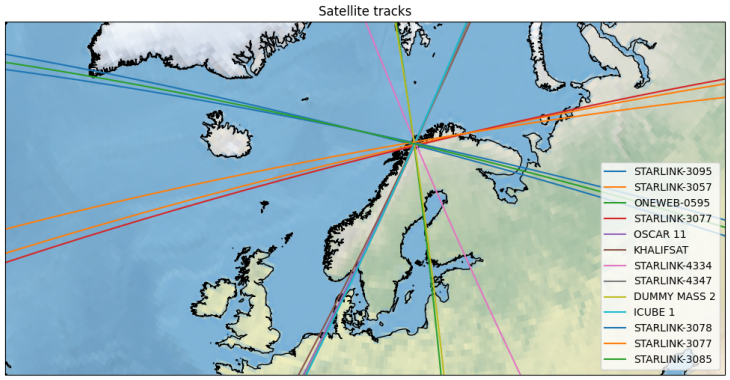

Figure 4.3: Closer view of satellite tracks

If a satellite is found in the data, its range over the entire time period it is detected is plotted. This is plotted together with the calculated distance between the specific satellite and the radar site over the same time period. The average difference between the range that is found using the radar data and the range that is found using satellite TLE data is calculated and plotted. The difference in time is also calculated and the graphs shifted in time so that their minimum points match. The plots of these satellites, with both the radar range and the TLE range, are shown in Figure 4.4. The time is determined by how long the radar detected the satellite, as this varies from satellite to satellite due to different orbits over the radar beam. Therefore this time from the radar measurements is used when also plotting the TLE altitude ensuring the same time period is covered with the same amount of points when finding the range difference. In Figure 4.4 the blue lines show the TLE range calculated and the orange lines show the detected radar range.

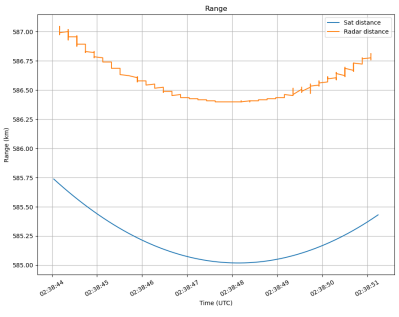

(a) STARLINK-3095

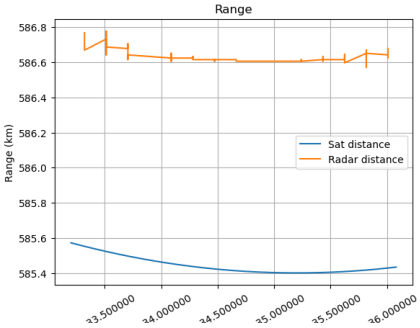

(b) STARLINK-3057

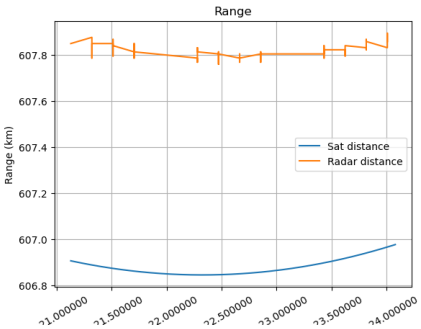

(c) ONEWEB-0595

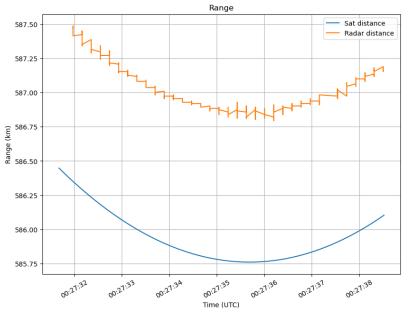

(d) STARLINK-3077

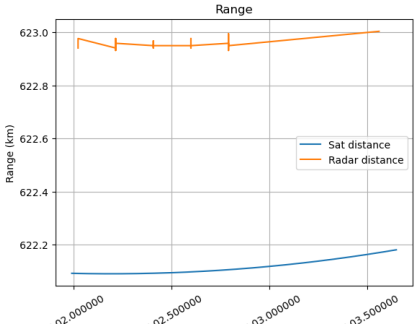

(e) OSCAR 11 (UoSAT 2)

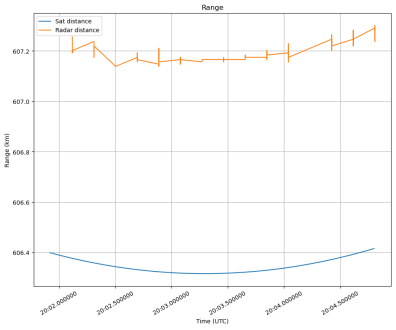

(f) KHALIFASAT

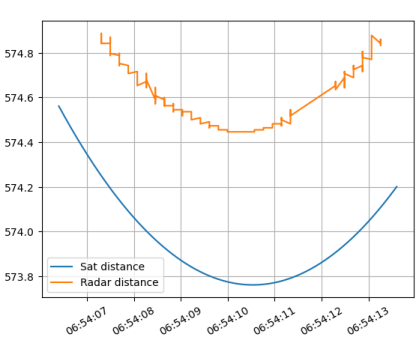

(g) STARLINK-4334

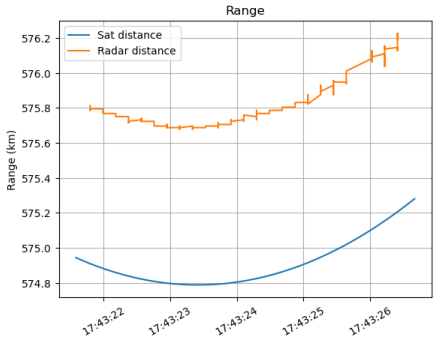

(h) STARLINK-4347

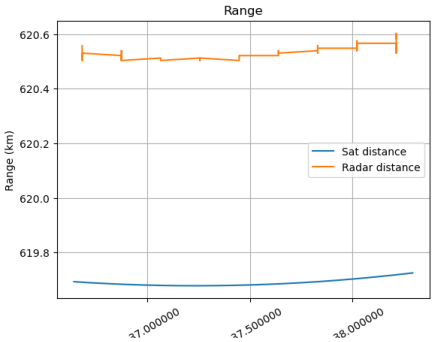

(i) DUMMY MASS 2

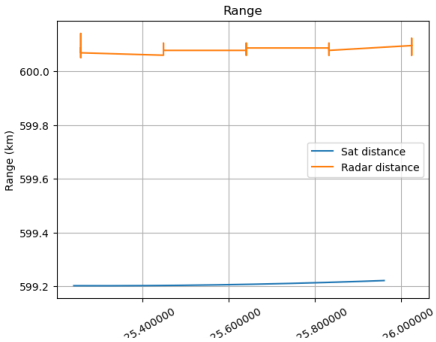

(j) ICUBE 1

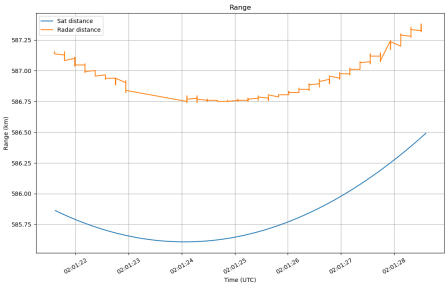

(k) STARLINK-3078

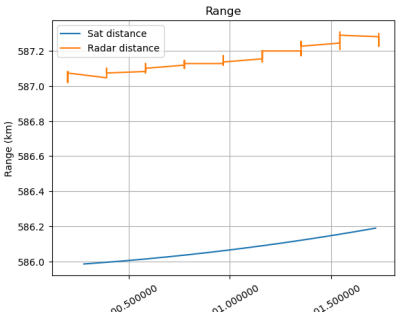

(l) STARLINK-3077

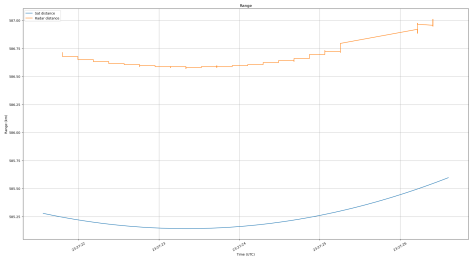

(m) STARLINK-3085

Figure 4.4: Range over time for radar data and TLE data. The blue lines show the range calculated from TLE data and the orange lines show the range measured by EISCAT UHF.

The vertical lines in the radar range that can be seen in the plots in Figure 4.4 is due to the values binning the nearest value to the satellite point.

The difference between the radar range found for the satellite and the range for the satellite found from the TLE is calculated for each point in the measured time. The average of this difference is found for each satellite. These values are shown in Figure 4.5 over the EISCAT UHF radar campaign time period. A red line shows the total average difference between the distances measured by the radar and from the TLE to be approximately 0.991 km.

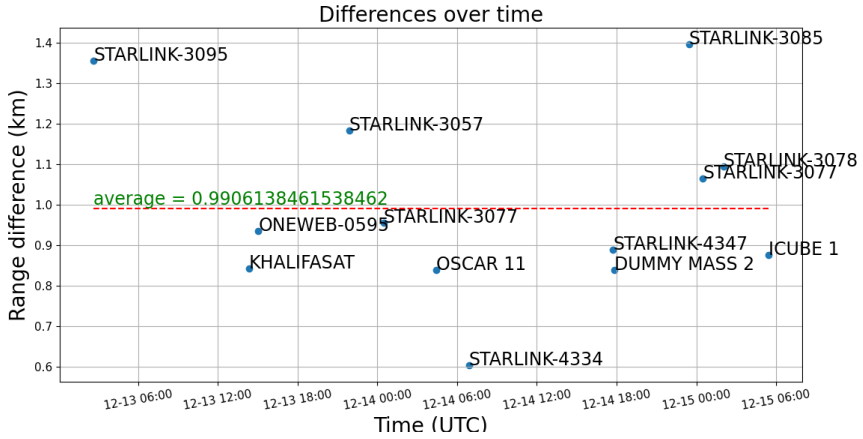

Figure 4.5: Average difference between radar measurements and satellite TLE calculations over the radar campaign period. The red line with following green text shows the average difference.

The average values seen in Figure 4.5 vary from satellite to satellite. One reason for this variation can be related to the type of satellite. The satellites that are found to deviate from the average the most are Starlink satellites, which can use active collision avoidance causing inaccurate TLEs. The shape of the satellite can also affect how the signal from the radar is reflected and detected. By not including the three Starlink satellites that can be seen in Figure 4.5 to be clearly higher than the other satellites, the offset found is 0.894 km. This could suggest that a more accurate offset is lower than the one found in Figure 4.5. For more accurate values, more satellites could be found and included in the calculations. This was not prioritized in this work, as the method is shown to work and the purpose of the calibration is to verify if a range offset is present in the EISCAT UHF radar measurements.

5

Meteor analysis method

In this chapter, the method for the second part of this thesis is presented. Section 5.1 explains the method used on the EISCAT UHF data obtained from the 2023 Geminids shower including how the approximate meteor position is calculated from only the EISCAT UHF data. Section 5.2 introduces the method for the MAARSY data, while Section 5.3 explains how the data from the two radars are used together to obtain accurate meteor positions together with RCS values for the simultaneous meteor observations.

5.1 EISCAT UHF data

The EISCAT UHF data is processed using the same method as described in Section 4.1 for this part of the work, although here including all data and ranges. Each day of the Geminids 2023 EISCAT UHF radar campaign is processed using the same code as in the calibration work. Once the processing is done for each of the individual days, the output is saved to HDF5 files. These files contain the detections that are made by the radar and that have a signal to noise ratio larger than an empirically determined threshold. When a signal is found that exceeds this threshold, interpolation is done for this particular pulse and the time, Doppler velocity, range and SNR are saved in the same HDF5 files. After they are all processed, these files are then input in bulk into a cluster code.

This cluster code finds a fitted trajectory to one meteor detection and then finds other detections that follow this fitted trajectory in the same time range as the first meteor detection. Each meteor detection has one chance to be associated with the other events. A variable called meteor number is assigned to the meteor. All detections that follow the same fitted trajectory are assigned the same meteor number. If the detection is not associated with any other events it is assigned the meteor number -1, indicating that this is not a detection following a meteor trajectory. The detection's meteor number, SNR, range, time and Doppler velocity and also the Doppler and range residual, which are the difference between the fitted trajectory and the measured trajectory, and fit parameters that are used in the cluster code are saved to a new HDF5 file.

The files are arranged such that the meteor numbers are repetitive, having the same length as the measured parameters. The parameters for the same meteor are therefore reachable through the use of the meteor numbers. The meteor number values can be used to index other values for every point of each meteor. How many points each meteor has depends on its trajectory through the EISCAT UHF beam and how long it was measured by the radar.

5.1.1 EISCAT UHF meteor position

The EISCAT UHF radar is a monostatic radar without interferometric capabilities and therefore an accurate position of a meteor can not be found with the EISCAT UHF radar alone. The only information about the position of the detection is that it is somewhere in the radar beam, but where in the beam is not known. A method for finding the position within the beam is described in Section 5.3.

It is possible to find approximate geographic coordinates for the meteor from the EISCAT UHF data using the elevation and azimuth for the radar during the campaign together with the measured range to the detection and the radar location.

First, the azimuth and elevation for the radar are used to find the meteor location in the local East-North-Up (ENU) coordinate system with origin at the EISCAT UHF site. The connection between the radar azimuth and elevation and the ENU coordinates for the meteor location is shown in Figure 5.1.

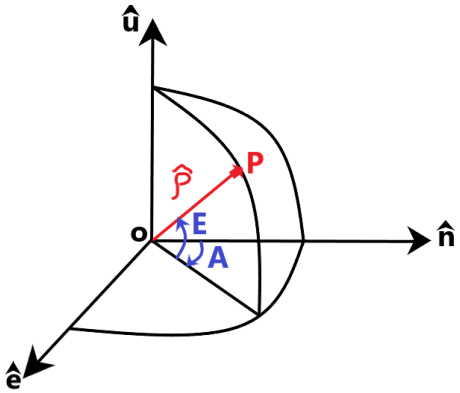

Figure 5.1: Connection between azimuth and elevation and ENU coordinates. Illustration made with inspiration from (ESA.int).

In Figure 5.1 E represents the elevation and A represents the azimuth for the radar. The point P in this case is the location of the meteor detection in ENU coordinates. The projection of the line of sight unit vector $\hat{\rho}$ seen in Figure 5.1 in each of the three ENU coordinates can be found from the azimuth and the elevation using the formulas (ESA.int)

$$\begin{gathered} \hat{\rho} \cdot \hat{e} = \cos(E) \cdot \sin(A) \\ \hat{\rho} \cdot \hat{n} = \cos(E) \cdot \cos(A) \longrightarrow \hat{\rho} \cdot \hat{s} = -\cos(E) \cdot \cos(A) \\ \hat{\rho} \cdot \hat{u} = \sin(E). \end{gathered} \tag{5.1}$$

In equation 5.1, the north unit vector $\hat{n}$ can also be expressed as the south unit vector $\hat{s} = -\hat{n}$. This is due to them both being tangents of the line representing the longitude for geographical coordinates, just opposite directions. The range to the meteor as measured by EISCAT UHF, R, can then be used to calculate the ENU coordinates using

$$\begin{aligned} e &= \cos(E) \cdot \sin(A) \cdot R \\ s &= -\cos(E) \cdot \cos(A) \cdot R \\ u &= \sin(E) \cdot R. \end{aligned} \tag{5.2}$$

Here, e is east, s is south, u is up and R is the one way range measured by the EISCAT UHF radar.

The next step is to transform the local ENU coordinates into Earth-Centered Earth-Fixed (ECEF) coordinates with origin at the center of Earth. The latitude

and longitude coordinates for the EISCAT UHF radar site are used in this transformation. Figure 5.2 shows the relationship between ENU coordinates and ECEF coordinates.

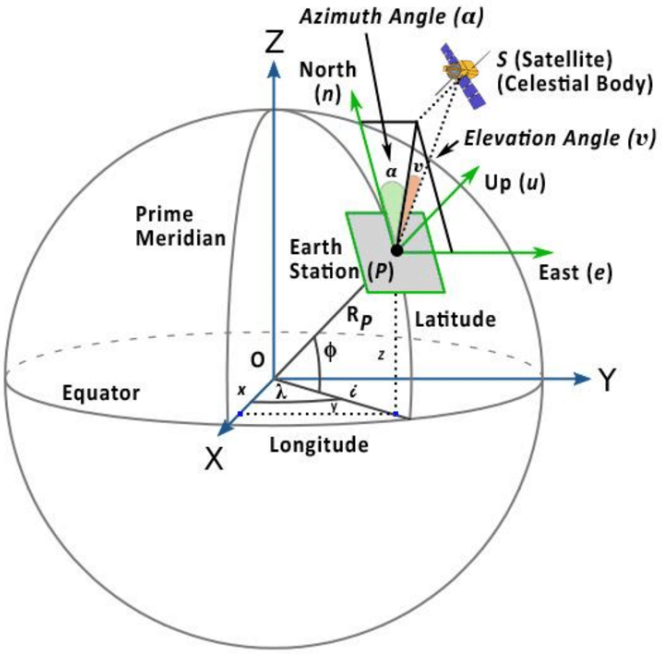

Figure 5.2: Illustration of the relationship between the ENU coordinate system and ECEF coordinates. R_p is the distance from the center of the Earth to the radar site, λ is the longitude, and ϕ is the latitude. Illustration taken from (Akhtaruzzaman et al., 2020).

In Figure 5.2 the represented local coordinate system is the ENU system. The ENU coordinates are related to ECEF coordinates by (Wikipedia.org)

$$\begin{bmatrix} \hat{x} \\ \hat{y} \\ \hat{z} \end{bmatrix} = \begin{bmatrix} \cos(\phi) \cdot \cos(\lambda) & \sin(\phi) \cdot \cos(\lambda) & -\sin(\lambda) \\ \cos(\phi) \cdot \sin(\lambda) & \sin(\phi) \cdot \sin(\lambda) & \cos(\lambda) \\ \sin(\phi) & -\cos(\phi) & 0 \end{bmatrix} \begin{bmatrix} \hat{u} \\ \hat{s} \\ \hat{e} \end{bmatrix} \tag{5.3}$$

where $(\hat{x}, \hat{y}, \hat{z})$ are the ECEF unit vectors, ϕ is the latitude and λ is the longitude as seen in Figure 5.2. The EISCAT UHF radar location in ECEF can be found from the known latitude and longitude coordinates with the relations (Zhu, 1994)

$$\begin{aligned} x &= (R+h)\cos(\phi)\cos(\lambda) \\ y &= (R+h)\cos(\phi)\sin(\lambda) \\ z &= (R+h-e^2R)\sin(\phi) \\ \text{where, } R &= a/(1-e^2\sin^2(\phi))^{1/2} \end{aligned} \tag{5.4}$$

where h is the altitude of the radar site normal to the ellipsoid, a is the ellipsoid equatorial radius given by $a = 6378.137$ km, e is the eccentricity given by $e^2 = 0.00669437999$ and b is the ellipsoid polar radius given by $b = a\sqrt{1-e^2}$ (Zhu, 1994). Denoting the ECEF coordinates for the EISCAT UHF radar location as (x_e, y_e, z_e), the approximate meteor location in ECEF coordinates can be expressed as

$$\begin{aligned} x &= x_e + \cos(\phi)\cdot\cos(\lambda)\cdot u + \sin(\phi)\cdot\cos(\lambda)\cdot s - \sin(\lambda)\cdot e \\ y &= y_e + \cos(\phi)\cdot\sin(\lambda)\cdot u + \sin(\phi)\cdot\sin(\lambda)\cdot s + \cos(\lambda)\cdot e \\ z &= z_e + \sin(\phi)\cdot u - \cos(\phi)\cdot s. \end{aligned} \tag{5.5}$$

Equation 5.5 gives the ECEF coordinates of the approximate meteor location found from the EISCAT UHF measurement. These coordinates are transformed into a geodetic coordinate system (longitude, latitude and altitude), by the use of relations described in Zhu (1994) and implemented in a script by Juha Vierinen, used in the code for the analysis in this thesies, seen in Appendix B.

5.1.2 EISCAT UHF analysis

Some analysis was done only on the EISCAT UHF data before the MAARSY data was available. The coordinate transformations described in Section 5.1.1 were used to obtain an approximate meteor position. By comparing the approximate meteor position to the location of MAARSY, an estimate of the number of meteors detected by both EISCAT UHF and MAARSY was found.

Some analysis was also done on the SNR. The SNR can contain information about the type of ablation the meteor undergoes as it moves through the atmosphere. A simple Gaussian function was fit to the SNR and the way that the SNR curve differed from the fit Gaussian curve gave information about the ablation processes. Further explanation of this analysis and results are shown in Section 7.1.

5.2 MAARSY method

The MAARSY data is processed through several software programs. Because of MAARSY's interferometric capabilities, the processing results in an accurate position for the meteor. The phase difference of the received signal between the different radar panels is used to determine the angle of arrival of the signal, and along with the range is used to determine the 3D location of the meteor.

This work focuses on the processing of the EISCAT UHF data and the comparison of MAARSY and EISCAT UHF data. Therefore the MAARSY processed data is provided and included in the work. A detailed description of MAARSY is provided in Latteck et al. (2012).

The position for the meteor detection is given in an ENU coordinate system with origin at the MAARSY radar site similar to the coordinate system described in Section 5.1.

From Figure 5.1 the elevation and azimuth angle of the meteor can be calculated from the ENU coordinates using (Akhtaruzzaman et al., 2020)

$$\begin{aligned} E &= \tan^{-1}\left(\frac{u}{\sqrt{e^2+n^2}}\right) \\ A &= \tan^{-1}\left(\frac{e}{n}\right) \end{aligned} \tag{5.6}$$

where E is the elevation, A is the azimuth and e, n, u are the east, north, and up coordinates of the meteor detection. The elevation and azimuth will be used to find the Cartesian coordinate position as described in Section 5.1.

5.3 EISCAT UHF and MAARSY

Since the EISCAT UHF radar measurements do not give any information about where in the radar beam the meteor is located, the MAARSY measurements are used to determine the accurate meteor position. Accurately positioning the meteor in the beam allows for determination of the RCS for EISCAT UHF. This procedure is explained here.

The files from the EISCAT UHF measurements and the MAARSY measurements from the same day are imported. The MAARSY files are looped through, and the times for the individual detections are used to find detections from the EISCAT UHF data in the same time interval.

To see if these measurements found in the same time interval are the same meteor measured by both radars, the distance to the EISCAT UHF radar site is compared. For EISCAT UHF, this distance is recorded as the range and can be used directly. For MAARSY, the meteor locations are saved as local ENU coordinates. These are transformed into ECEF coordinates and added to the ECEF coordinates of the MAARSY radar site to give the meteor location in ECEF coordinates. The distance between the EISCAT UHF radar and the meteor detected by MAARSY is found by calculating the difference between the MAARSY meteor coordinates and the EISCAT UHF radar site coordinates, both in the ECEF coordinate system. This distance is compared to the recorded EISCAT UHF meteor range. If the ranges are similar, they are considered to be the same meteor.

By finding the difference between the range to the meteor as measured by EISCAT UHF and the distance between EISCAT UHF and the meteor as measured by MAARSY, it is investigated if there is a range offset, in general, between the measurements. This offset is compared to the range offset found in the calibration work from Section 4.2. A polynomial is fit to both the EISCAT UHF and MAARSY ranges to obtain more accurate calculations due to noise in some measurements.

5.3.1 Meteor location in EISCAT UHF beam

From this point in the analysis, the MAARSY meteor location is assumed to be correct. This assumption will be used to find a more accurate meteor location in the EISCAT UHF beam. A description of the method used follows. This method can be used on every dual-detected meteor.

A unit vector in the direction of the EISCAT UHF radar beam is made to represent the k-vector direction. The coordinates for the radar site together with the azimuth and elevation for the campaign are used to transform this vector into ECEF coordinates. First, the azimuth and elevation are transformed to ENU coordinates with equation 5.2. These ENU coordinates are then, together with the radar site coordinates, transformed into ECEF coordinates using equation 5.5.

The measurements of the meteor positions can contain some noise, so a second order polynomial is fit to the x, y and z coordinates for the meteor trajectory to reduce the effect of the noise. The time for both the EISCAT UHF measurement and the MAARSY measurement are normalized by subtracting the mean value of the time. This is due to the time being in Unix time, which is seconds elapsed since Unix epoch on 1 January 1970 00:00:00 UTC (Unixtimestamp.com). The time therefore contains large numbers which will cause problems when fitting

the second order polynomial to the time and position, so the mean time is subtracted to obtain the normalized time. The normalized position vector for MAARSY detections is calculated at both the EISCAT UHF and MAARSY observation times by dividing each direction by the length of the position vector.

The angle between the EISCAT UHF k-vector and the normalized position is found by taking the inverse cosine of the dot product between the two vectors, both for the EISCAT UHF observation times and for the MAARSY observation times:

$$\text{radar boresight angle} = \arccos(\text{k-vec} \cdot \text{normalized meteor pos}). \tag{5.7}$$

The angles calculated using the EISCAT UHF observation times represent the meteor angle away from the middle of the main beam (the boresight angle), with an angle of o° being in the middle of the beam.

These angles give information about where the meteor is in the EISCAT UHF beam and allows finding the radar gain at a specific angle using the beam pattern in Figure 3.2.

An expression for the RCS is given in equation 2.2. For EISCAT UHF, the received power from a meteor detection P_r is given by (Kero et al., 2008b)

$$\begin{aligned} P_r &= T_{met} \cdot k_B \cdot b_w \\ \text{where, } T_{met} &= SNR \cdot T_{sys} \\ \rightarrow P_r &= SNR \cdot T_{sys} \cdot k_B \cdot b_w \end{aligned} \tag{5.8}$$

where SNR is the signal to noise ratio measured by the radar, T_{met} is the signal temperature of the meteor, T_{sys} is the system temperature which is monitored during the experiment, k_B is the Boltzmann constant and b_w is the receiver bandwidth, calculated from the pulse length p_l as $b_w = 1/p_l = 1/146.4\mu s = 6830.60$ Hz. The noise in the meteor analysis is defined by the total pulse length because it is based on the noise power in the frequency bin size which is defined by this total pulse length.

The RCS for EISCAT UHF can then be calculated from equation 2.2 as

$$\sigma = \frac{(4\pi)^3 \cdot R^4 \cdot SNR \cdot T_{sys} \cdot k_B \cdot b_w}{G(\theta)^2 \cdot \lambda^2 \cdot P_t} \tag{5.9}$$

where $G(\theta)$ is the radar gain at the specific angle away from antenna boresight. This is the radar gain found using the EISCAT UHF beam pattern and MAARSY to locate the meteor within the beam.

Equation 5.9 is used to find the RCS for the EISCAT UHF measurements and compare these with the RCS from MAARSY measurements, which is found while processing the MAARSY data and stored in the data files.

6

Statistic analysis

In this chapter, the statistics of the EISCAT UHF data and the coincidence EISCAT UHF and MAARSY data are presented. Section 6.1 presents the total meteor events detected by the EISCAT UHF radar during the 2023 Geminids campaign together with the number of meteor events estimated to be detected simultaneously in the two radars and the number of meteor events actually found in both EISCAT UHF and MAARSY. Section 6.2 consists of histogram presentations of the meteor altitude, meteor Doppler velocity and meteor SNR from the data presented in Section 6.1. All these histograms consist of values from the EISCAT UHF radar.

6.1 EISCAT UHF-MAARSY Meteor Coincidence

Table 6.1 summarizes the number of meteors that were found in EISCAT UHF and MAARSY data during the 2023 Geminids campaign. Each meteor consists of a different number of data points. In Table 6.1, the meteors are categorized based on the number of data points. The number of meteors found in EISCAT UHF data from each range of data points is shown in the second column. As explained in Section 5.1.1, the EISCAT UHF data is used to obtain an approximate meteor location, which is compared to the location of the MAARSY radar. If the meteor's coordinates in latitude and longitude fall within the empirically determined coordinate interval representing the MAARSY beam, we expect to see the meteor in MAARSY. The number of meteors seen by EISCAT

UHF and expected to be seen by MAARSY is shown in the third column. Finally, the number of meteors actually seen by both MAARSY and EISCAT UHF is shown in the fourth column. To be clear, both the third and fourth columns are subsets of the second column.

Table 6.1: Number of meteors found in EISCAT UHF and MAARSY data, categorized by the number of data points in the meteor. The percentage presented in the last two columns is calculated from the second column.

Nr. data points	Found EISCAT	Expected in MAARSY	Found MAARSY
Larger than 4	2990	511 (17,1%)	1172 (39%)
Larger than 7	2456	432 (17,6%)	1048 (43%)
Larger than 10	2048	371 (18,1%)	931 (45%)
Total number	3258	550 (16,9%)	1218 (37%)

Comparing the third and fourth columns in Table 6.1, there are many more meteors seen simultaneously by both MAARSY and EISCAT UHF than expected. This means that the coordinates used in determining the width of the MAARSY radar field-of-view were underestimated. Since the number of meteors expected in MAARSY was only used to get an idea of the number of dual-detections when working with only EISCAT UHF data the underestimation will not affect the work.

The total count of meteors in the EISCAT UHF data for each day is shown in the blue bins in Figure 6.1. Each bin represents one hour. The red bins are the expected count of meteors dual-detected in both EISCAT UHF and MAARSY. The meteor count shows a uniform distribution of meteors across all days of the radar campaign, even though the Geminids meteor shower peak was expected to be around the last two days. Sporadic meteors are the explanation for this uniformity, as they constitute a large part of the meteor flux entering the atmosphere every day.

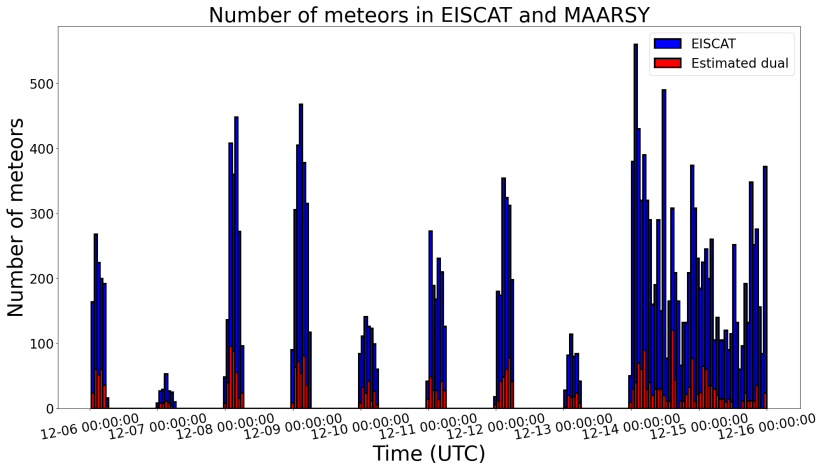

Figure 6.1: Total meteor counts per day binned by hour shown in blue. Count of meteors estimated to be detected in both EISCAT UHF and MAARSY shown in red.

Figure 6.1 thus displays clearly the prevalence of the sporadic meteors, as the Geminids meteor shower peak is not large enough to exceed the sporadic meteors.

Figure 6.2 shows a more detailed count for the last two days in the radar campaign, as the radars were operated continuously these days. The hourly count for the last two days roughly follows the hourly count from the previous days, not indicating a meteor shower peak.

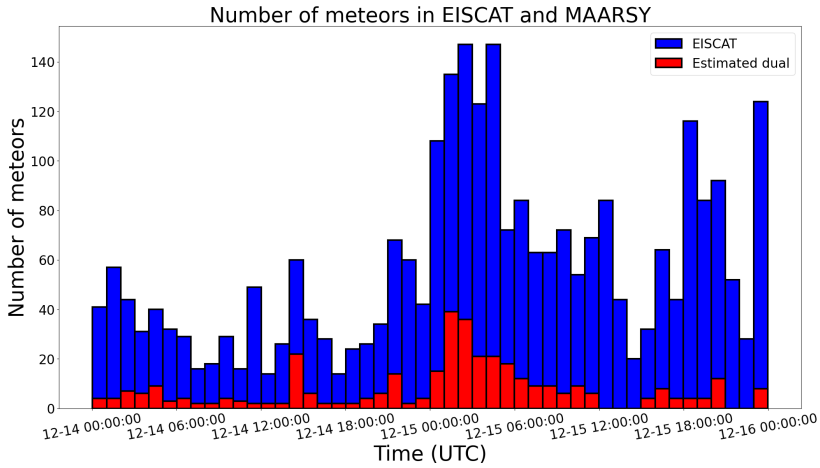

Figure 6.2: More detailed presentation of the last two days in the campaign, with each bin representing one hour.

Figure 6.3 shows the number of meteors that are detected in both EISCAT UHF and MAARSY in green bins together with the number of meteors detected by only EISCAT UHF in blue bins over the full length of the EISCAT UHF campaign period. The blue bins are the same as in Figure 6.1 and 6.2.

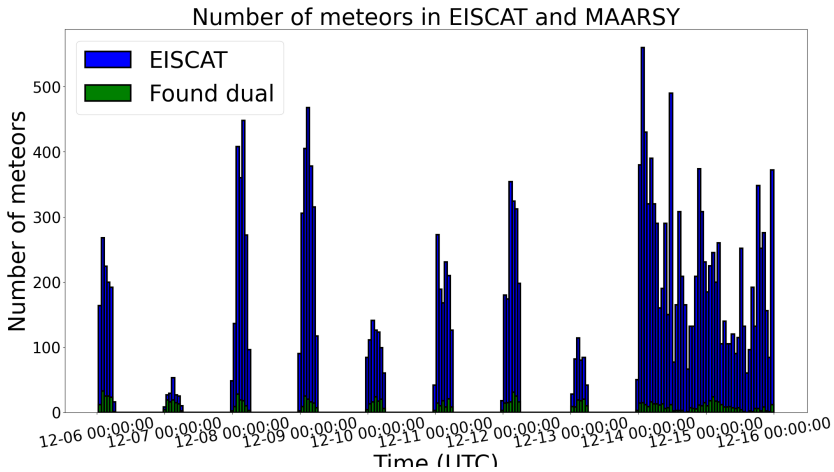

Figure 6.3: The number of meteors detected by both EISCAT UHF and MAARSY for the full length of the campaign.

Figure 6.4 show a more detailed view over the last two days in Figure 6.3.

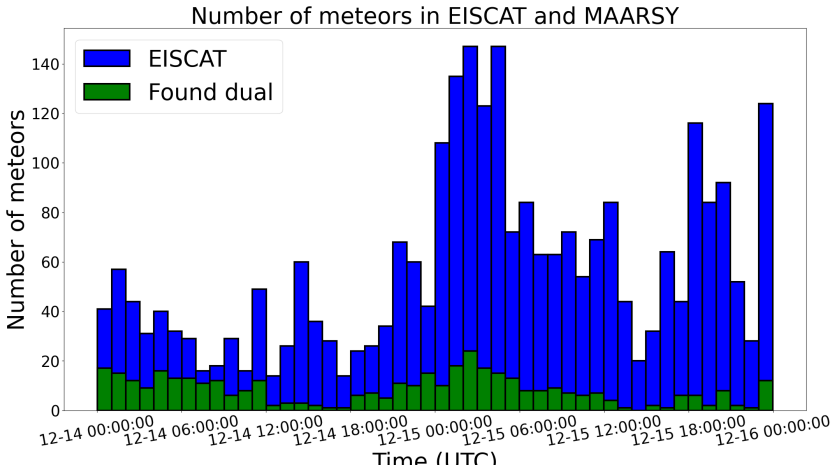

Figure 6.4: The number of meteors detected by both EISCAT UHF and MAARSY for the last two days of the campaign.

Figure 6.3 follow the same distribution as Figure 6.1, with an approximately constant meteor count every day over the entire radar campaign.

6.2 Histograms

Before further analysis of the meteors in Table 6.1, the dataset is first simplified. Meteors seen by EISCAT UHF with 4 or less data points are excluded from the analysis. This is done to remove the events that do not have enough data to be a good representation of the meteor. At this early stage in the analysis, the goal was to include a reasonably high number of meteors which could be filtered out at a later stage if they are deemed not useful.

Figures 6.5, 6.6 and 6.7 show histograms of the altitude, Doppler velocity and SNR respectively of the remaining meteors in Table 6.1. In each figure, the blue histograms show the meteors seen by EISCAT UHF (the second column in Table 6.1), the red histograms show the meteors seen by EISCAT UHF that are expected to be seen by MAARSY (the third column), and the green histograms show the meteors actually seen by EISCAT UHF and MAARSY simultaneously (the fourth column).

Figure 6.5 shows the altitude distribution of the meteors. During the campaign, the EISCAT UHF radar pointing direction intersected with the MAARSY beam at around 100 km altitude. This was done because this altitude around 100

km is the most interesting when looking at meteor ablation, as can be seen in Figure 2.1 showing the altitudes at which different metals ablate. Figure 6.5 shows that a high number of meteor events with an altitude around 100 km are dual-detected by EISCAT UHF and MAARSY, confirming the intersection point of the beams from the two radars. It can also be seen that EISCAT UHF detects meteors along more of the beam than just the intersection altitude.

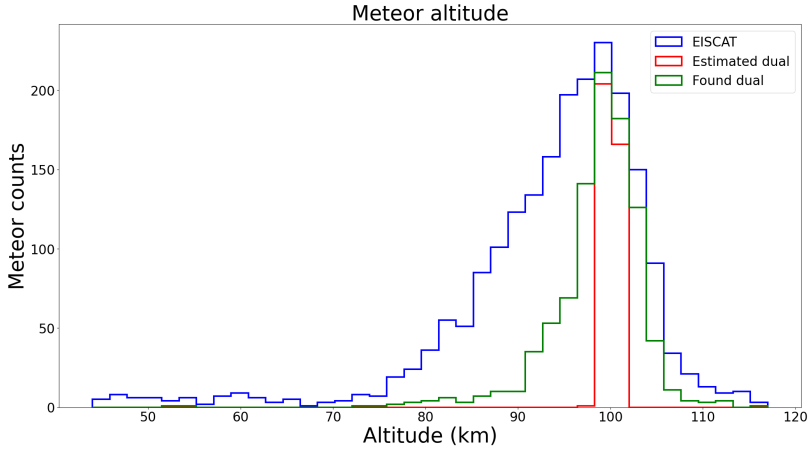

Figure 6.5: The meteor altitude observed by EISCAT UHF.

Figure 6.6 shows the Doppler velocity distribution of the meteors observed by EISCAT UHF, for the total EISCAT UHF count, the dual-detected meteors and the expected dual-detected meteors. Also for the dual-detected meteors, the EISCAT UHF Doppler velocity is presented. This Doppler velocity is only the line-of-sight velocity with respect to the EISCAT UHF radar. At low Doppler velocities, the number of meteors detected by EISCAT UHF is much larger than the number of dual-detected meteors. At higher Doppler velocities, above approximately 10 km/s, the number of meteors detected by EISCAT UHF and the number of dual-detected meteors follow a more similar distribution, indicating they are made up of mostly the same meteors. The high EISCAT UHF count for lower Doppler velocities could be explained by events detected closer to the EISCAT UHF beam, so not over the MAARSY beam and therefore at a lower altitude, indicating lower Doppler velocity. Meteors with lower velocity will ablate, and hence be detected by the radar, at lower altitudes. As seen in Figure 6.5, the meteors detected by only EISCAT UHF covers a lower altitude than the dual-detected meteors due to the intersection, which could explain the lower Doppler velocity counts for EISCAT UHF.

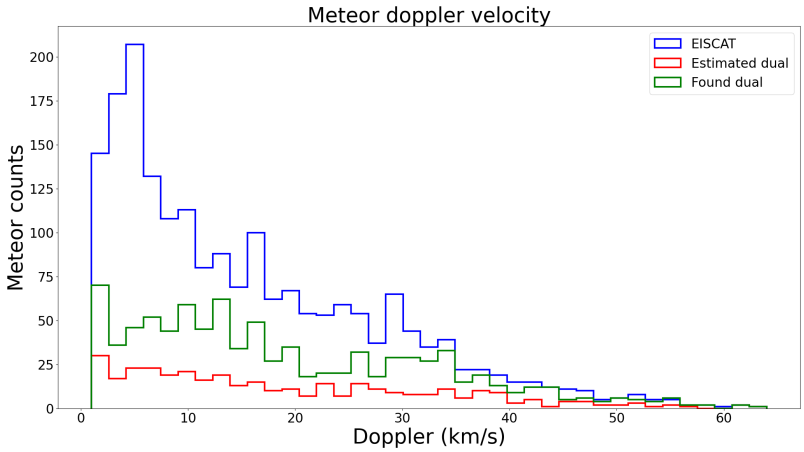

Figure 6.6: The Doppler velocity from meteors observed by EISCAT UHF.

Figure 6.7 shows the EISCAT UHF SNR distribution of the total meteor count, the dual-detected meteors and the expected dual-detected meteors. All three of the functions have a peak around 30 dB followed by a decrease in value.

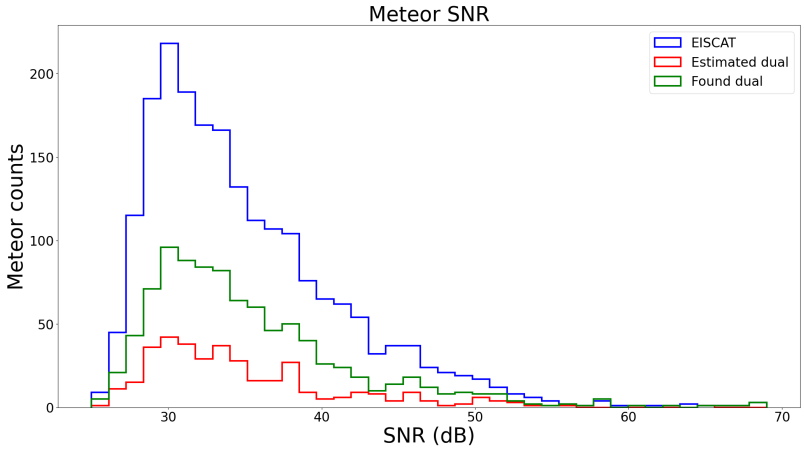

Figure 6.7: The meteor SNR observed by EISCAT UHF.

As seen in Figures 6.5 to 6.7, the number of expected dual-detected meteors are consistently lower than the number of actually dual-detected meteors. This is the same underestimation that is shown in Table 6.1 due to underestimation of MAARSY beam width.

7

Analysis and discussion

In this chapter, the results from the meteor classification method developed in Chapter 5 are presented and discussed together with case studies of dual-detected meteor events. Section 7.1 presents the results of the classification together with some examples of events classified as each of the three atmospheric processes investigated in this work. Section 7.2 contains examples and verification of the calibration work that was presented in Chapter 4, here with data from both the EISCAT UHF radar and the MAARSY radar. In Section 7.3, case studies of meteors undergoing simple ablation, differential ablation and fragmentation are presented and discussed.

7.1 Meteor classification

One of the goals in this work was to find a method to classify meteor fragmentation and different types of meteor ablation events. The different processes are explained in Section 2.3.1. Initially, the EISCAT UHF SNR was used to do a general classification. The SNR was, in each individual pulse sequence, calculated for each pulse and for each pulse with an SNR over an empirically determined threshold. The combined SNR from each pulse found to be detecting the same meteor represents the SNR measurements for that meteor event.

The SNR characteristics were used to do a simple classification of the meteor events. The goal of this first classification was to do a general classification that

could at a later point be improved. Some of the events are long and include signal from one or more of the side lobes of the radar, while most of them only include signal from the main lobe. Therefore, a Gaussian function was used to fit to the SNR, as a Gaussian is a good fit for the main beam of EISCAT UHF. The difference between the original SNR function and the Gaussian fit was found and the gradient of this difference taken. This was done to find any sudden drops or increases in the SNR of the signal that could differentiate between simple ablation and differential ablation. To also classify fragmentation events, a Fourier transform was performed on the gradient of difference between the SNR function and the Gaussian fit function. The expected 'beat pattern' associated with fragmentation could be approximated to a sinusoidal function and the Fourier transform of a sinusoidal function gives two peaks symmetric around zero frequency.

If the SNR curve follows the antenna pattern, and in this case the Gaussian fit, it is assumed to be a case of simple ablation. If the SNR curve has a clear drop, but follows the antenna pattern before and after this drop, the event is assumed to be a case of differential ablation. However, the case of fragmentation is more complicated. The SNR varies for most of the meteor events but with different rates and shapes. To find the events with an approximately sinusoidal SNR shape, their Fourier transform is used to find peaks indicating this sinusoid.

At this point, a stricter threshold is applied to decide which meteor events to include in this analysis. Only meteor events that contain more than 10 data points are included in this analysis. If the meteors have fewer than 10 points, the pattern in the SNR is more difficult to detect. Since the form of the SNR is the whole foundation of this classification, it was decided that using SNR curves with many data points was more important than including more short meteors, which would also have proved more difficult to use later in the analysis.

From examining the SNR behaviour, the limits for determining which kind of process a particular meteor had undergone were determined. For determining which meteors could have undergone differential ablation, the average value of the gradient of the difference between the SNR function and the Gaussian fit was determined. If between one and seven points deviated from this average by more than an empirically decided upon value of 2, the meteor was assumed to be a case of differential ablation. The one-to-seven range of the number of points deviating from the average comes from a manual studying of the plots, as the meteors that clearly had a drop in SNR went back to follow the previous SNR curve after just a few points. This will be seen clearly later in this section. If the event had more than seven points outside the average, it varied overall throughout the detection and did not have the characteristic clear drop. A meteor event was assumed to undergo simple ablation if there were no points

deviating more than the threshold value of 2 from the average. These events follow the Gaussian fit and therefore are events only within the main lobe, as longer events that are detected in the side lobes will not follow the simple fit. There are only a few of these events in this analysis and therefore the side lobes are not considered, although these events are likely to have had the highest SNR. These events could be analysed by applying a more complex fit than a Gaussian. The events that did not fulfill the previous limits, and had a peak in the Fourier transform due to their periodic structure, were determined to be fragmentation events.

A summary of the results of this classification process is shown in Table 7.1. The process was repeated on different sets of meteor events, presented as the rows in Table 7.1: all events detected by EISCAT UHF in total, only events possibly seen by MAARSY, all events with more than 10 data points and events possibly seen by MAARSY with more than 10 points.

Table 7.1: Classification of meteor events using their SNR

Meteor events included	Diff. ablated	Simple ablated	Fragmented
All meteors, all points	548	1002	1708
Possibly MAARSY, all points	111	172	267
All meteors, >10 points	489	933	626
Possibly MAARSY, >10 points	102	159	110

Table 7.1 shows that from this SNR classification, the fewest meteor events are classified as differential ablated events, while simple ablated events and fragmented events vary depending on which data is included.

Figures 7.1 to 7.3 show examples of events classified by this method. Each figure contains the same three plots. The leftmost plot is the SNR recorded over the meteor time duration, shown by blue dots, together with the Gaussian fit, shown by the green line. The middle plot is the gradient of the difference between the SNR and the Gaussian fit (both seen in the leftmost plot). This gradient is shown by the blue line. The average value of the gradient is shown by the center red line, while the two red and dotted lines, one above and one below the average, show the ± 2 deviation threshold from the average. If no points of the gradient are beyond these lines, the meteor is considered to undergo simple ablation. If between one and seven points of the gradient are beyond these lines, differential ablation is assumed. As many as seven points are chosen to ensure all meteor events that undergo differential ablation are included. The rightmost plot is the Fourier transform of the gradient of the difference between the SNR plot and the Gaussian fit. The peaks in this determine if the meteor event is classified as fragmentation.

Figure 7.1 shows a meteor event classified as simple ablation. The SNR plot follows the Gaussian fit and no outlier values can be seen in the gradient of the difference between SNR and the Gaussian fit - every point is within the threshold lines. The Fourier transformation shows no clear peaks and this event is therefore classified as simple ablation and not fragmentation.

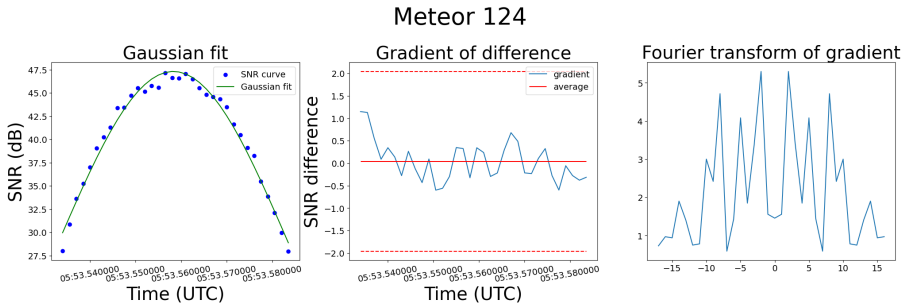

Figure 7.1: Example of one event classified as simple ablation.

Figure 7.2 shows a meteor event classified as differential ablation. A drop in SNR is seen just past the midpoint in time. After this drop, the signal resumes following the same form as before the drop. The gradient of the difference between SNR and the Gaussian fit contains two points below the low threshold line, which is why this is classified as differential ablation.

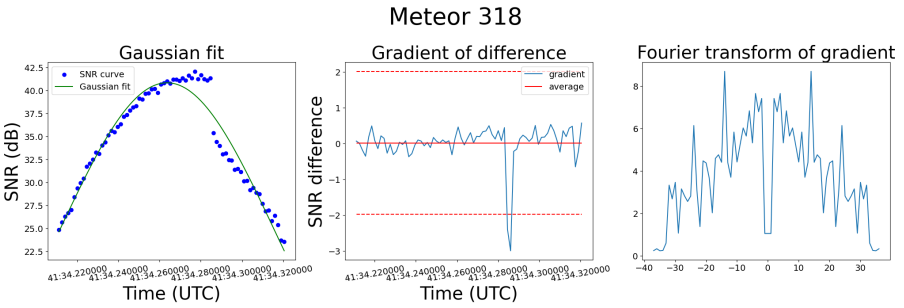

Figure 7.2: Example of one event classified as differential ablation.

Figure 7.3 shows a meteor event classified as fragmentation. These events are not as straightforward to classify - the SNR can vary for many reasons, as the meteor is moving and is not uniform in size. The SNR follows a Gaussian fit well, similar to simple ablation, but the Fourier transformation in the third picture shows clear peaks which are not seen in the simple ablation case. This event is classified as fragmentation because of the distinct peaks in the Fourier

transform. An approximate sinusoidal shape of the gradient can also be seen in the middle plot which causes these peaks in the Fourier transform.

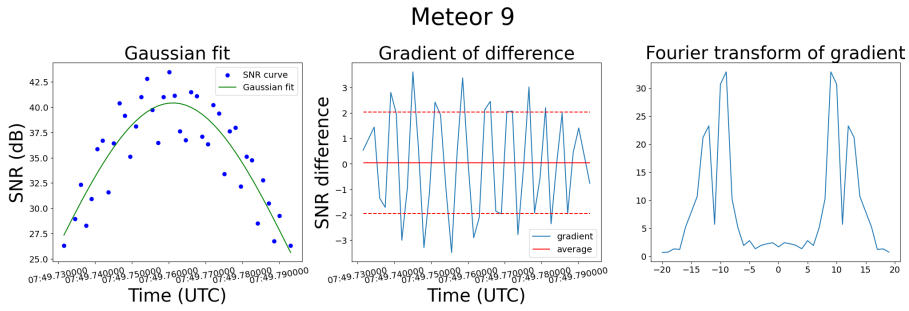

Figure 7.3: Example of one event classified as fragmentation.

Meteors can also undergo different processes at the same time. This is beyond the scope of this work, where the meteors are assumed to only undergo a single process.

Figure 7.4 shows one example of a meteor that passed through two sidelobes in addition to the main lobe. In this case, the simple Gaussian function used for the fit is not sufficient, and this method will not classify these events in an accurate way. To classify these events with this method, the beam pattern of the EISCAT UHF radar could be used in place of a Gaussian when fitting a curve to the SNR. Alternatively, only using the meteor echoes corresponding to the main lobe would allow the Gaussian to still be used, at the cost of losing some data points.

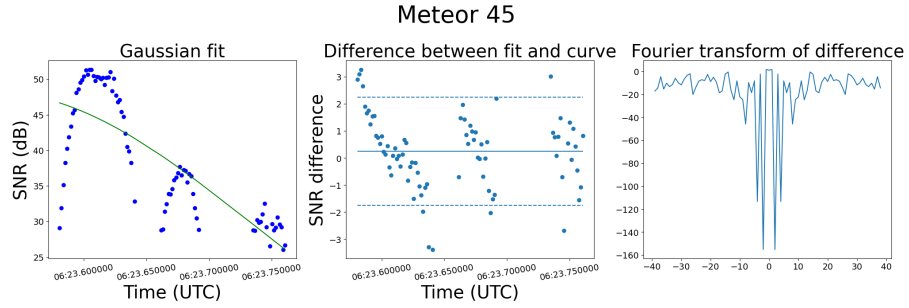

Figure 7.4: Example of one event including radar side lobs

7.2 Calibration work

The range from EISCAT UHF to the meteor is thought to be inaccurate, as described and investigated in Section 4.1. To compare the range found by EISCAT UHF with the range found by MAARSY, first the distance from the MAARSY measurement of the meteor to the EISCAT UHF radar site was found. In this way, independent measurements of the same range are compared and an offset between the measurements is easier to find.

For every dual-detection across the full length of the campaign, the average difference in ranges was found. If the average difference was over 3 km, it was assumed that the radars did not detect the same meteor or the detections were inaccurate. Without including the average differences over 3 km, the average of the average differences was found and applied as a calibration factor. A histogram of the average differences before and after applying the calibration can be seen in Figure 7.5.

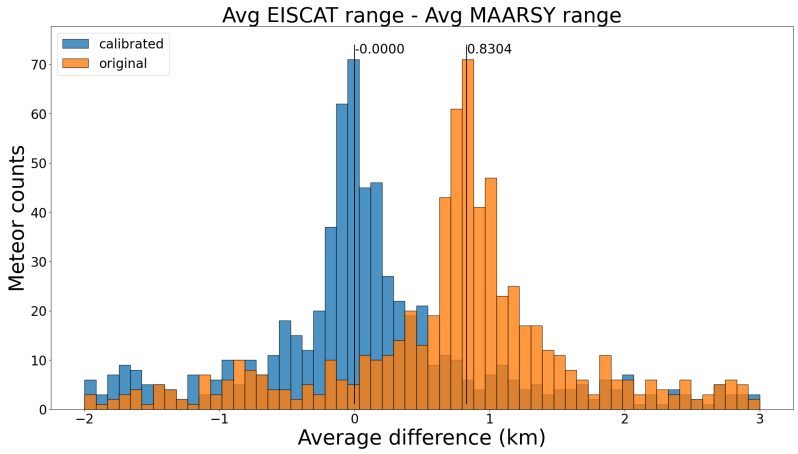

Figure 7.5: Difference between EISCAT UHF and MAARSY range measurements. Orange bins show the difference before the calibration value is applied and the blue bins show the difference after the calibration value is applied. The number by each vertical line is showing the average difference over all meteors for each case.

As seen in the blue histogram in Figure 7.5, the difference between the ranges measured by EISCAT UHF and the ranges measured by MAARSY center around 0 when a calibration factor of 0.8304 km is applied on the EISCAT UHF measurements. Figure 4.5 shows that when all the satellites found in the work are included, an offset of 0.9791 km is found. This is larger than the offset found by using the two radars. This could be explained by drifting or orbit

adjustments of satellites after the TLE epoch time. When not including the Starlink satellites, which have a large effect on the calculation of the offset, the offset from the satellite calibration work is 0.8940 km, closer to the 0.8304 km found by using the two radars. A more detailed analysis would be beneficial to obtain an accurate offset for the EISCAT UHF UHF range, but it is clear that an offset in the range should certainly be taken into account.

Both the satellite and the meteor processing use the raw complex voltage data. This offset found in the raw data may be accounted for when the data analysis package GUISDAP processes EISCAT UHF data. As the documentation for the EISCAT data is ambiguous, it was necessary to investigate and validate the timing. When processing the raw complex voltage data, 122 samples of the transmitted pulses are used. The transmit pulse is recorded in a 128 sample set, but the pulse is only in 122 of those values. Instead of starting the processing at the sixth sample, as done in this work, the processing could start from the zeroth sample, which might account for this offset. The approximate offset when skipping the first five samples can be found by $r = c \cdot t/2$, where c is the speed of light, and $t = 1.2\,\mu s \cdot 5$ samples, where the sample spacing is $1.2\,\mu s$. This gives $r = 900$ m, which corresponds fairly well with the previous offset values found.

Figures 7.6 and 7.7 show two examples of the range of dual-detected meteor events without and with applying the calibration factor. Both these examples show the overall trend that the EISCAT UHF range measurements are higher than the MAARSY range measurements. This is the case for the measurements where both the radars measure the meteor at the same time, as in Figure 7.6, and for the measurements where one of the radars detects the meteor first, and the other radar later in the meteor trajectory, as in Figure 7.7.

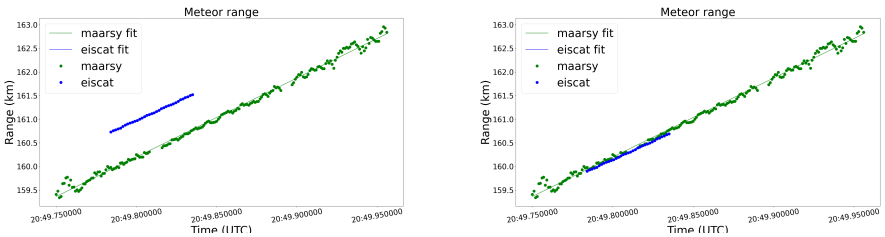

(a) Not calibrated event **(b)** Calibrated event

Figure 7.6: A dual-detected meteor event where both EISCAT UHF and MAARSY measure the meteor at the same time. Blue dots represent EISCAT UHF measurements, while the blue line represents the fitted EISCAT UHF range. Green dots represent MAARSY measurements, while the green line represents the fitted MAARSY range.

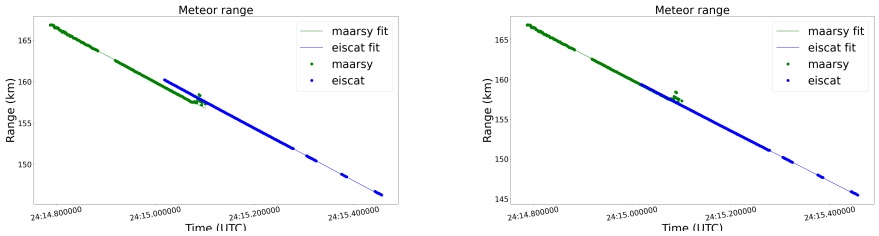

(a) Not calibrated event **(b)** Calibrated event

Figure 7.7: A dual-detected meteor event where EISCAT UHF measures the meteor after MAARSY. Blue dots represent EISCAT UHF measurements, while the blue line represents the fitted EISCAT UHF range. Green dots represent MAARSY measurements, while the green line represents the fitted MAARSY range.

For the rest of the work a range offset of 0.8304 km is applied to the EISCAT UHF data.

7.3 Meteor events

7.3.1 EISCAT UHF RCS

The EISCAT UHF RCS is calculated using equation 5.9. The constant values used in this work for this equation can be seen in Table 7.2.

Table 7.2: Constant values used in the calculation of EISCAT UHF RCS

Variable	Value
k_B	$1.380649 \cdot 10^{-23} m^2 kg/s^2 K$
λ	0,322 m
P_t	$1.2 \cdot 10^6 W$
$T_s ys$	100 K
b_w	6830.60 Hz

T_{sys} and P_t are measured continuously during radar operation. Their values shown in Table 7.2 are an average of the measured values. $G(\theta)$ is found by using values from Figure 3.2 for the boresight angles found by using MAARSY data. SNR and R (range) in equation 5.9 are values from the radar measurements. Both $G(\theta)$, SNR and R change for each point at which the RCS is evaluated.

7.3.2 Simple Ablation

Meteors experiencing simple ablation will have smooth SNR curves as they experience a constant mass loss over time. Because of this constant mass loss the RCS will stay mostly constant throughout the meter event observation. An example of a dual-detected simple ablation meteor event is shown in Figure 7.8.

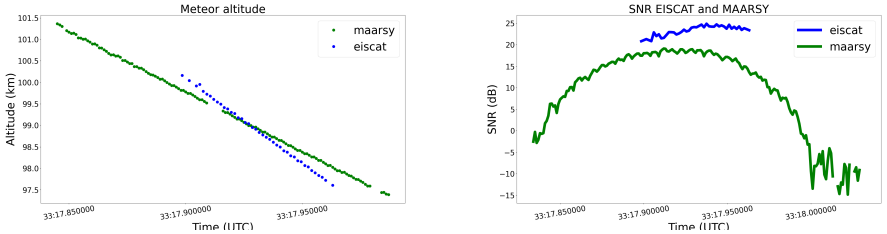

(a) Meteor altitude

(b) SNR for meteor duration

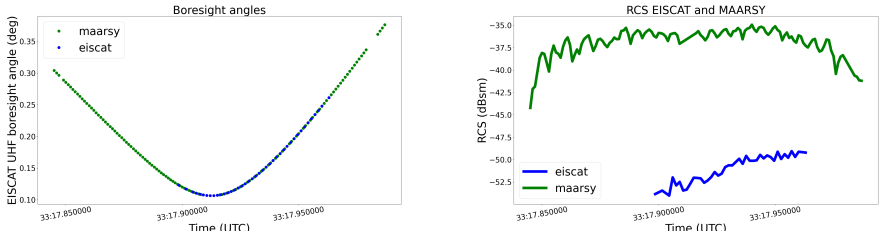

(c) Angle from boresight

(d) RCS for meteor duration

Figure 7.8: Example of a meteor event experiencing simple ablation. EISCAT UHF detections are shown in blue and MAARSY detections are shown in green. Each subfigure includes a caption describing what is plotted.

Figure 7.8a shows the meteor altitude as calculated by both the EISCAT UHF radar (blue) and the MAARSY radar (green). The range offset factor found in Section 7.2 is applied to the EISCAT UHF data before the altitude is calculated. The detections follow the same trajectory and are detected at the same times. MAARSY has a larger field-of-view and therefore detects the meteor for a longer time period. Figure 7.8c shows the angles from boresight of the EISCAT UHF radar, calculated for the detections from both radars. An angle of 0° means that the meteor passes through the middle of the beam, which is not the case for this detection as the lowest angle is around 0.1°. However, the entire EISCAT UHF measurement is inside the mainlobe of the radar. Figure 7.8b shows the SNR curve from both radars. Figure 7.8d shows the RCS curve that is calculated using the SNR and the angle off boresight in Figure 7.8c to find the position of the meteor in the EISCAT UHF beam.

The SNR is relatively smooth for both radars together with an approximate

constant RCS, showing the simple ablation. The angular gain for EISCAT UHF can sometimes be underestimated due to inaccurate angles found at some individual points when comparing the locations detected by EISCAT UHF and MAARSY. This can cause some inaccuracies in the RCS values. However, the RCS is a good representation of the meteor behaviour when the overall curve is analysed.

7.3.3 Differential ablation

A meteor experiencing differential ablation is characterised by a sudden drop in the SNR curve. An example of a dual-detected differential ablation meteor event is shown in Figure 7.9.

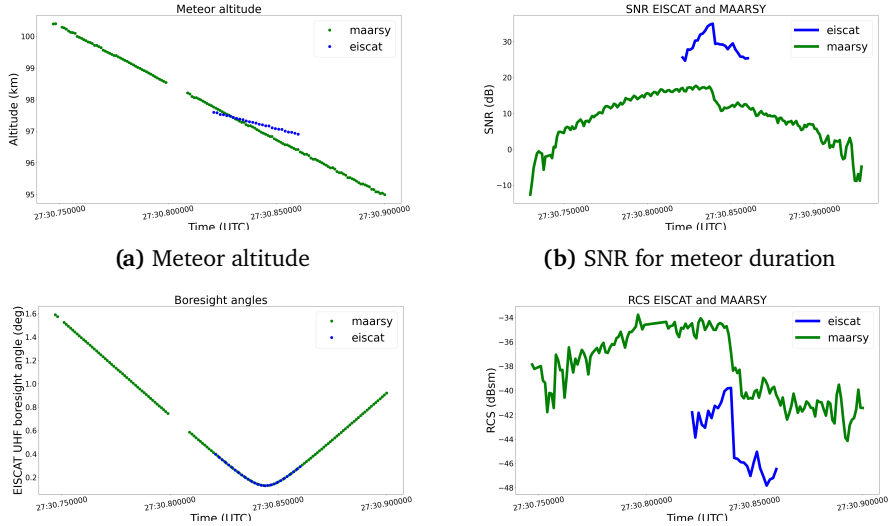

(a) Meteor altitude

(b) SNR for meteor duration

(c) Angle from boresight

(d) RCS for meteor duration

Figure 7.9: Example of one meteor event experiencing differential ablation. EISCAT UHF detections are shown in blue and MAARSY detections are shown in green. Each subfigure includes a caption describing what is plotted.

Figure 7.9a shows the meteor altitude as calculated by both the EISCAT UHF radar and the MAARSY radar. Figure 7.9c shows that the meteor goes through the EISCAT UHF mainbeam for the full EISCAT UHF measurement duration, while it goes through one sidelobe in MAARSY, seen by the gap in the green MAARSY points.

Figure 7.9b shows the SNR curves for EISCAT UHF and MAARSY. A clear drop can be seen approximately in the middle of both the measurements. In Figure

7.9d, the RCS curves display this drop even more clearly. The RCS is relatively constant for both of the radars before dropping several dBsm, after which it remains relatively constant again. The drop indicates the ablation of the particles with less heat-resistance. When the less heat-resistant particles ablate completely, the meteor size becomes smaller, hence the lower RCS value.

The altitudes at which the RCS profiles for both EISCAT UHF and MAARSY experienced drops indicative of differential ablation is shown in Figure 7.10. It is seen that the RCS tends to suddenly drop between roughly 95 and 105 km altitude. Comparing these measured differential ablation altitudes with the predicted ablation altitudes in Figure 2.1 shows good agreement and supports the method used to classify differential ablation.

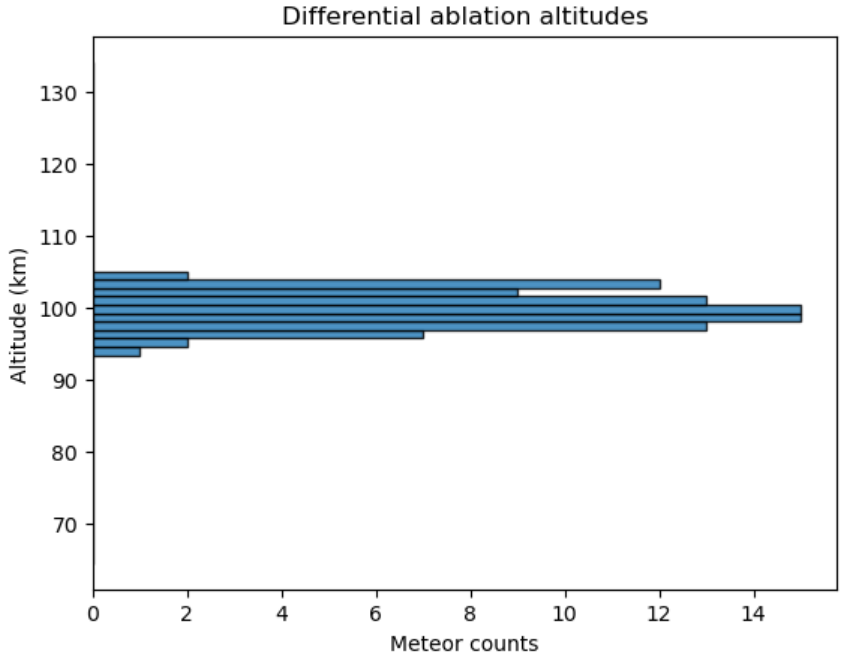

Figure 7.10: The altitudes where the dual-detected meteors experience differential ablation determined from RCS values.

Figure 2.1 shows that K and Na ablate between roughly 97 and 102 km altitude for a meteor with the most likely mass and velocity predicted by the CABMOD model (Plane, 2012). Figure 7.10 has good agreement with this altitude interval. The slightly larger altitude interval in Figure 7.10 can be explained by the fact that the meteors detected by the radar are unlikely to be of the same mass and velocity as the example meteor in the CABMOD model.

The same altitude interval presented in Figure 7.10 can be seen together with the mean altitude of the total meteors that are detected by both EISCAT UHF and MAARSY.

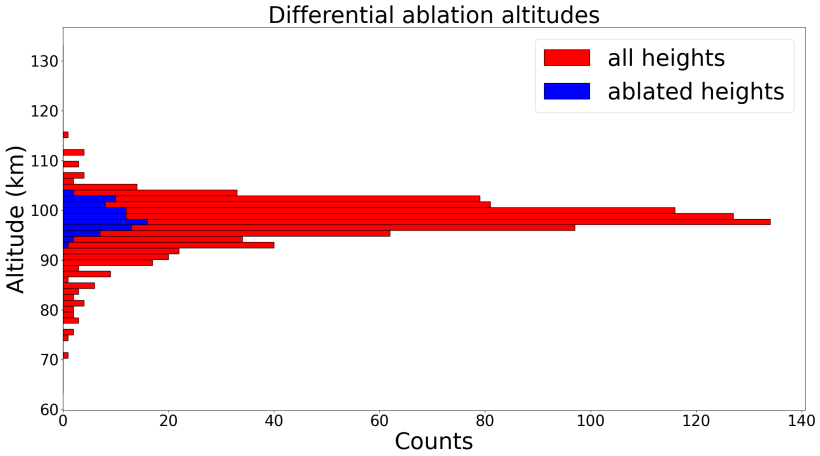

Figure 7.11: The altitudes where the dual-detected meteors experience differential ablation determined from RCS values in blue together with the mean altitudes for all dual-detected meteors in red.

The RCS is used to get a good estimate of the differential ablation drop, and calculation of the RCS requires using MAARSY to locate the meteor within the EISCAT UHF beam. This means that only the meteors detected by both EISCAT UHF and MAARSY are included. The EISCAT UHF radar is pointed such that the intersection altitude with the MAARSY beam is around 100 km. Therefore the altitude interval given in Figure 7.10 could be artificially limited by the interval in altitude where the two beams intersect. However, it was seen in Figure 6.5 that there are dual-detected meteors with both lower and higher altitudes than the minimum and maximum altitudes in Figure 7.10. Figure 7.11 also confirms this, by the representation of the mean altitudes for all meteors that are dual-detected. In general, the dual-detected meteors have altitudes between 85 and 110 km. This interval is larger than the altitude interval of 95 to 105 km found for differential ablation and thus is good evidence that the altitude interval found for differential ablation is not artificially limited by the intersection point of the two radar beams. In turn, this further supports that Figure 7.10 shows the altitudes where the meteors experience differential ablation.

The EISCAT UHF SNR was used to investigate whether a similar altitude interval for differential ablation can be seen when a drop in the SNR (instead of the RCS) is used as a indicator for the process. When using the SNR, all

of the EISCAT UHF data can be used, as MAARSY is not required to located the echo in the EISCAT UHF beam. Figure 7.12 shows the altitude distribution where the meteors detected by EISCAT UHF experienced a drop in SNR. This distribution covers a larger altitude interval than the one found by RCS, from around 80 km to 110 km with the main count located around 100 km. Unlike the interval found using RCS, this is a larger altitude interval than the one expected from the differential ablation theory and Figure 2.1.

One explanation for this larger altitude interval using the EISCAT UHF SNR to identify the differential ablation altitude is a highly variable SNR value. The RCS, when the meteor is experiencing differential ablation, will have a lower value after the drop and stay approximately constant at this lower value, as can be seen in Figure 7.9d. This is because the RCS represents the ability of the radar to detect the meteor. When one or several of the constituents of the meteor completely ablate, the meteor will be smaller and the radars ability to observe the meteor (thus the RCS) will be lower. Conversely, the SNR follows the radar beam pattern and will therefore not have a constant value after the drop, seen in Figure 7.9b. For some EISCAT UHF meteor events the SNR will have a decreased value while following the radar beam shape, while others have approximately the same SNR value shortly after the drop. When using the classification method for differential ablation explained in Section 7.1, some meteors will have a gradient that exceeds the threshold in only a couple of points. An example of this is shown in Figure 7.2. Other meteors that also experience differential ablation have a relatively large number of points exceeding the threshold. These meteors could simply have a strong variation in SNR instead of experiencing differential ablation.

The altitudes in Figure 7.12 that fall outside the expected differential ablation interval could be explained by the inclusion of these meteors that do not experience differential ablation. However, excluding these meteors also excludes some meteor events that do undergo differential ablation. The value for the number of points the gradient can exceed the threshold is found empirically. It was decided to choose a value that includes all meteor events undergoing differential ablation, and hence also some that do not. This choice is made because of the importance the differential ablation events have in this work.

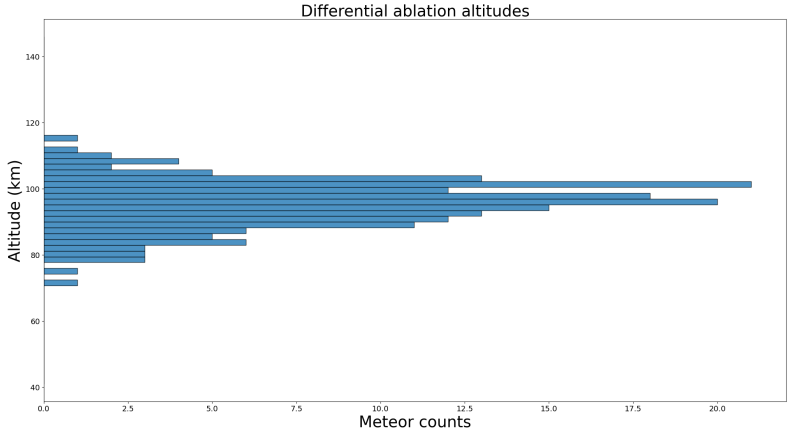

Figure 7.12: The altitudes where the dual-detected meteors experience differential ablation determined from EISCAT UHF SNR values.

Figure 7.13 shows the same altitude where the meteor experience ablation as Figure 7.12 together with the mean altitude value for the total count of EISCAT UHF detected meteors. This figure shows that the mean altitude of the total count of meteors has a much larger range interval than Figure 7.12, suggesting that the ablated altitudes found in Figure 7.12 supports the ablation theory.

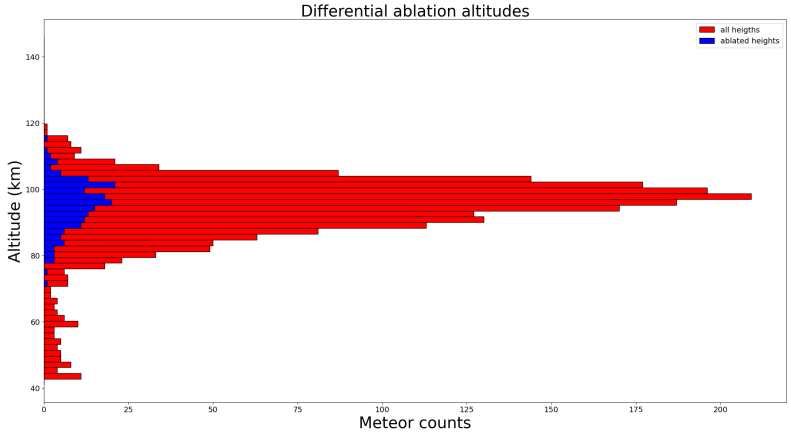

Figure 7.13: The altitudes where the dual-detected meteors experience differential ablation determined from EISCAT UHF SNR values in blue together with the mean altitudes for all dual-detected meteors in red.

Both when using EISCAT UHF and MAARSY RCS and when using EISCAT UHF SNR to determine the differential ablation heights, most differential ablation happens around 100 km altitude, which is consistent with Figure 2.1. Due to different meteor masses and velocities than the theoretical model used to calculate the ablation profiles the results vary. However, it is clear that a large quantity of the meteor events experiencing differential ablation do this around 100 km altitude, indicating complete ablation of K and Na.

7.3.4 Fragmentation

Fragmentation can be seen as a beat pattern in the pulse integrated SNR and hence also in the RCS, as described in Section 2.3.1. Figure 7.14 shows one example of a clear beat-like oscillating pattern associated with fragmentation. This pattern is measured by both EISCAT UHF and MAARSY.

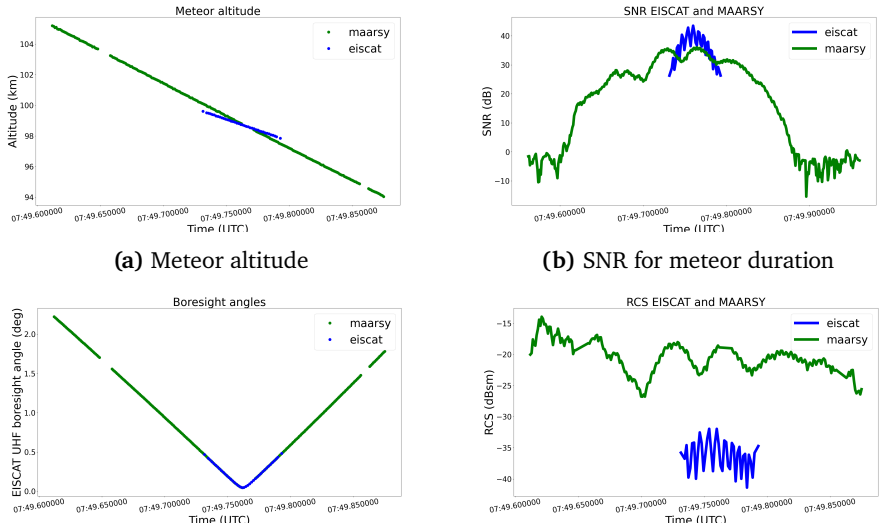

(a) Meteor altitude

(b) SNR for meteor duration

(c) Angle from boresight

(d) RCS for meteor duration

Figure 7.14: Example of one meteor event experiencing fragmentation. EISCAT UHF detections are shown in blue and MAARSY detections are shown in green. Each subfigure includes a caption describing what is plotted.

The beat pattern caused by in-phase and out-of-phase scattering is seen in both the SNR and the RCS for both radars. The sinusoidal pattern has different frequencies for the different radars. This is because EISCAT UHF and MAARSY have different operating frequencies. EISCAT UHF has a higher frequency, hence a smaller wavelength, and the beat pattern will oscillate quickly. MAARSY has a lower frequency, hence a larger wavelength, resulting in a slower oscillation

frequency. This can be seen clearly in Figure 7.14b and 7.14d. Towards the end of the MAARSY observation time, the frequency is seen to decrease. However, the meteor observation stops before a clear decreasing pattern is measured.

Figure 7.15 shows another example of fragmentation detected in both EISCAT UHF and MAARSY data.

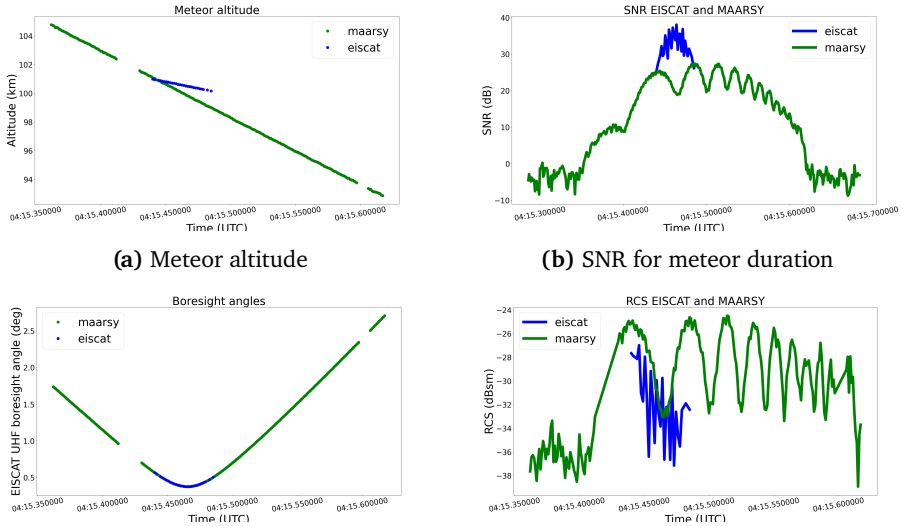

(a) Meteor altitude

(b) SNR for meteor duration

(c) Angle from boresight

(d) RCS for meteor duration

Figure 7.15: Example of one meteor event experiencing fragmentation. EISCAT UHF detections are shown in blue and MAARSY detections are shown in green. Each subfigure includes a caption describing what is plotted.

The example in Figure 7.15 also has the characteristic oscillation pattern for both radars, with a higher frequency in EISCAT UHF than in MAARSY due to the difference in wavelength. In this example, the oscillation pattern is observable for a long time period in the MAARSY data and can be seen to increase in frequency as the time passes. This could be due to the difference in velocities between the fragments increasing. We assume that the fragments have the same or nearly the same velocity upon fragmentation. If one of the fragments has a lower deceleration than the other, the difference in velocity between fragments will increase with time, resulting in a higher frequency oscillation pattern with time. This could explain the increase in the beat pattern frequency seen in the MAARSY RCS in Figure 7.15d.

8

Conclusion

This thesis had two main goals. The first goal was to confirm the accuracy of the EISCAT UHF range measurements, which was also the topic of the project paper. This was a fundamental part of this thesis, as the second main goal was to investigate, via dual-detections by the EISCAT UHF radar and the MAARSY radar, the different processes a meteor undergoes in the atmosphere.

The TLEs for satellites with orbits passing over the EISCAT radar site during the EISCAT UHF 2022 Geminids campaign were found. TLEs give information about the satellites' orbital elements which are used to find the range from the satellite to the radar at the time of closest approach. This time of closest approach, together with the range found from the TLEs, helped determine which radar data files, and which timestamps and ranges in those files, could contain the satellites.

From comparing the range to the satellite measured by the radar and the range found from the satellite TLE, it was found that the radar overestimates the range and an offset of 0.991 km is required. Due to a lack of detailed information regarding the satellites and their orbital manoeuvres during the TLE epoch time, this range offset contains some uncertainty. The range offset was reduced by 0.1 km, to 0.894 km, when the three Starlink satellites, which were the three satellites that deviated most from the mean range, were excluded.

By comparing the range to a meteor measured by the EISCAT UHF radar from the EISCAT radar site to the distance between the same meteor and the EISCAT

radar site as measured by the MAARSY radar, a similar range offset was found with the value of 0.830 km. This offset was applied to the EISCAT UHF radar range when working towards the second main goal in this work. The EISCAT UHF radar and the MAARSY radar simultaneously observed the 2023 Geminids meteor shower, with intersecting fields-of-view around 100 km altitude. Dual-detected meteors found from this campaign were used to investigate the second main goal of this thesis.

The development of a method for automatically classifying meteor ablation types using the meteor's SNR was pursued. This included the use of signatures in the SNR that are present in signal reflected from simple ablation, differential ablation and fragmentation. Differential ablation contains clear signatures and were correctly classified at the highest rate. Simple ablation and fragmentation were less successful because meteors exhibit different signatures based on their sizes and velocities. However, in several meteor events, fragmentation with a distinctive beat pattern from two or more fragments moving at different velocities was observed.

In general, the RCS shows clearer signatures of the different ablation types than the SNR. Through the use of the MAARSY meteor position, the location of the meteor in the EISCAT UHF beam could be found and from this the EISCAT UHF RCS calculated. Case studies were performed on three individual meteor events: one representing simple ablation, one representing differential ablation and one representing fragmentation.

These case studies showed the signatures of the processes in both the SNR and the RCS for measurements from both radars. Differential ablation could be seen by a clear drop at the same point in time for both EISCAT UHF and MAARSY. For all events detected, both by using the dual RCS observations and using the EISCAT UHF SNR, the altitudes of this differential ablation correspond to the approximate theoretical ablation altitude for K and Na. One of the factors that can cause some deviation in the differential ablation height is the velocity of the meteors. Correlations between differential ablation altitudes and meteor velocities are a promising avenue of research to further pursue with this dataset. This provides experimental evidence that these constituents completely ablate at around 100 km altitude.

Two cases for fragmentation were analysed. Both cases show a beat pattern in both the SNR and RCS for both radars, with different oscillation frequencies due to the different radar wavelengths. One event shows an approximately constant oscillation frequency through the majority of the observation time, with an indication of a decreasing frequency towards the end. The other event shows an increasing oscillation frequency in the MAARSY SNR and RCS, as this radar has a longer observation time and will observe the meteor event

longer than the EISCAT UHF. This increase in frequency implies one of the fragments has a higher acceleration than the other, as the distance between the fragments increases at an increasing rate.

This work can be continued by using the RCS from the two radars to find mass estimates for the meteor events. This can be used to investigate further details in the ablation and fragmentation processes, for example by determining the size of the two or more pieces present during a fragmentation event. The meteor trajectories can also be found and give information about the different sources of the meteors, allowing characterization of meteor mass by source. The method for characterizing differential ablation meteor events through the SNR can, for future work, be applied to a larger dataset, for instance the EISCAT VHF radar, which contains hundreds of hours of data in a zenith, or vertical, beam orientation over multiple years.

Bibliography

18th Space Control Squadron. Spaceflight safety handbook for satellite operators. URL https://www.space-track.org/documents/Spaceflight_Safety_Handbook_for_Operators.pdf.

M. Akhtaruzzaman, S. Bari, S. A. Hossain, and M. Rahman. Link budget analysis in designing a web-application tool for military x-band satellite communication. 47(17-33), 2020. doi: 10.47981/j.mijst.08(01)2020.174(17-33).

celestis.com. What are the "azimuth and elevation" of a satellite? URL https://www.celestis.com/resources/faq/what-are-the-azimuth-and-elevation-of-a-satellite/.

S. Close, M. Oppenheim, S. Hunt, and L. Dyrud. Scattering characteristics of high-resolution meteor head echoes detected at multiple frequencies. *J. Geophys. Res.*, 107(A19), 2002. doi: 10.1029/2002JA009253.

EISCAT.se. Tromsø. URL https://eiscat.se/about/sites/eiscat-tromso-site/.

ESA.int. Transformations between ecef and enu coordinates. URL https://gssc.esa.int/navipedia/index.php/Transformations_between_ECEF_and_ENU_coordinates.

J. D. Garrillo-Sánchez, D. Nesvorný, P. Pokorný, D. Janches, and J. M. C. Plane. Sources of cosmic dust in the earth's atmosphere. *Geophys. Res. Lett*, 43(1): 11,979–11,986, 2016. doi: 10.1002/2016GL071697.

J. Kero, C. Szasz, A. Pellinen-Wannberg, G. Wannberg, A. Westman, and D. D. Meisel. Three-dimensional radar observation of a submillimeter meteoroid fragmentation. *Geophysical Research Letters*, 35(4), 2008a. doi: 10.1029/2007GL032733.

J. Kero, C. Szasz, G. Wannberg, A. Pellinen-Wannberg, and A. Westman. On the meteoric head echo radar cross section angular dependence. *Geophysical*

Research Letters, 35(7), 2008b. doi: doi.org/10.1029/2008GL033402.

D. Koschny, R. H. Soja, C. Engrand, G. J. Flynn, J. Lasue, A.-C. Levasseur-Regourd, D. Malaspina, T. Nakamura, A. R. Poppe, V. J. Sterken, and J. M. Trigo-Rodríguez. Interplanetary dust, meteoroids, meteors and meteorites. *Space Sci Rev*, 215, 2019. doi: 10.1007/s11214-019-0597-7.

R. Latteck, W. Singer, M. Rapp, B. Vandepeer, T. Renkwitz, M. Zecha, and G. Stober. Maarsy: The new mst radar on andøya—system description and first results. *Radio Science*, 47(1), 2012. doi: doi.org/10.1029/2011RS004775.

L. Limonta, S. Close, and R. A. Marshall. A technique for inferring lower thermospheric neutral density from meteoroid ablation. *Planetary and Space Science*, 180(1), 2020. doi: 10.1016/j.pss.2019.104735.

A. Malhotra and J. D. Mathews. A statistical study of meteoroid fragmentation and differential ablation using the resolute bay incoherent scatter radar. *Journal of Geophysical Research*, 116(A04316), 2011. doi: 110.1029/2010JA016135.

R. A. Marshall and S. Close. An fdtd model of scattering from meteor head plasma. *Journal of Geophysical Research: Space Physics*, 120(5931–5942), 2015. doi: 10.1002/2015JA021238.

MITHaystack. Digitalrf. URL `https://github.com/MITHaystack/digital_rf`.

E. Murad and I. P. Williams. *Meteors in the Earth's Atmosphere*. Cambridge University Press, Cambridge, United Kingdom, 2002.

NASA.gov. Geminids, a. URL `https://science.nasa.gov/solar-system/meteors-meteorites/geminids/`.

NASA.gov. Meteors and meteorites, b. URL `https://science.nasa.gov/solar-system/meteors-meteorites/`.

J. Plane. Cosmic dust in the earth's atmosphere. *Chem Soc Rev*, 41:6507–6518, 2012. doi: 10.1039/c2cs35132c.

rhodesmill.org. Elegant astronomy for python. URL `https://rhodesmill.org/skyfield/`.

M. A. Richards. *Fundamentals of radar signal processing*. McGraw-Hill Ecucation, New York, 2014.

P. J. Rousseeuw and C. Croux. Alternatives to the median absolute deviation.

Journal of the American Statistical Association, 88(424):1273–1283, 1993. doi: 10.1080/01621459.1993.10476408.

C. Schult, J. Kero, G. Stober, and P. Brown. Dual frequency measurements of meteor head echoes simultaneously detected with the maarsy and eiscat radar systems. *Icarus*, 355(114137), 2021. doi: 10.1016/j.icarus.2020.114137.

L. K. Tarnecki, R. A. Marshall, G. Stober, and J. Kero. Meteoroid mass estimation based on single-frequency radar cross section measurements. *Journal of Geophysical Research: Space Physic*, 126, 2021. doi: 10.1029/2021JA029525.

Unixtimestamp.com. Unix. URL `https://www.unixtimestamp.com/`.

Vierinen(2021). Signal processing. URL `http://kaira.uit.no/fys2006`.

Wikipedia.org. Spherical coordinate system. URL `https://en.wikipedia.org/wiki/Spherical_coordinate_system`.

J. Zhu. Conversion of earth-centered earth-fixed coordinates to geodetic coordinates. *IEEE Transactions on Aerospace and Electronic Systems*, 30(3):957–961, 1994. doi: 10.1109/7.303772.

A

Satellites

Satellites that were found to have an orbit passing over the EISCAT radar site during the time period the EISCAT UHF radar was running in the 2022 Geminids campaign.

Table A.1: All satellites that are found having an orbit passing over the EISCAT radar site during the 2022 Geminids campaign. The time is time of closest approach, altitude the altitude of the satellite found at this time, together with the latitude and longitude coordinates for this time. The satellites are sorted after their TLE epoch time.

Satellite	Time (UTC)	Alt (km)	Lat (°)	Lon (°)
ANDESITE	2022-12-13 17:25:48	598.65	69.45	19.25
WISE	2022-12-13 07:47:24	459.30	69.51	19.13
SPACEBEE-67	2022-12-13 08:31:24	460.12	69.37	19.10
STARLINK-3095	2022-12-13 02:38:48	574.58	69.50	19.15
FLOCK 4P 6	2022-12-13 10:05:48	457.05	69.73	19.30
FLOCK 4V 2	2022-12-13 10:18:00	509.46	69.68	19.36
STARLINK-3057	2022-12-13 21:53:36	574.40	69.56	19.39
COSMOS 1674	2022-12-13 06:25:36	487.23	69.51	19.25
PUJIANG 1 (PJ-1)	2022-12-13 05:41:24	450.79	69.71	19.33
ONEWEB-0595	2022-12-13 15:02:24	613.37	69.46	19.10
FLOCK 4EP 8	2022-12-13 19:11:00	480.98	69.31	19.38
PRATHAM	2022-12-14 08:07:12	664.74	69.32	19.14
STARLINK-3077	2022-12-14 00:27:36	575.03	69.46	19.37
OSCAR 11	2022-12-14 04:27:00	619.93	69.73	19.23

KOMPSAT 3	2022-12-14 01:48:00	698.05	69.38	19.15
SPACEBEE-123	2022-12-13 14:54:48	493.37	69.46	19.35
JILIN-01-10	2022-12-13 11:54:36	523.48	69.67	19.38
AIM	2022-12-14 00:56:48	506.59	69.77	19.31
FLOCK 4S 38	2022-12-13 18:46:36	505.41	69.71	19.22
KHALIFASAT	2022-12-13 14:20:00	590.58	69.80	19.35
FORMOSAT 3D	2022-12-14 10:01:36	709.01	69.76	19.22
NUSAT-27	2022-12-14 10:57:00	488.41	69.33	19.32
STARLINK-4334	2022-12-14 06:54:12	565.06	69.70	19.35
TIGRISAT	2022-12-14 02:58:36	628.94	69.65	19.22
STARLINK-4347	2022-12-14 17:43:24	564.54	69.54	19.24
FLOCK 4S 41	2022-12-14 09:29:36	502.96	69.33	19.23
FLOCK 4S 41	2022-12-14 18:48:12	502.96	69.41	19.32
SICH-2-1	2022-12-14 19:18:00	531.93	69.51	19.25
SDSAT	2022-12-14 20:07:12	469.17	69.56	19.20
NUSAT-13 EMMY	2022-12-14 10:13:48	446.71	69.71	19.37
DUMMY MASS 2	2022-12-14 17:48:36	620.98	69.65	19.12
LEMUR 2 YNDRD	2022-12-15 03:50:00	515.69	69.48	19.37
SHERPA-FX2	2022-12-14 23:38:48	529.71	69.77	19.29
IRIDIUM 51	2022-12-15 02:21:12	468.15	69.57	19.23
FLOCK 1C 8	2022-12-15 03:38:48	581.71	69.39	19.39
ICUBE 1	2022-12-15 05:25:24	571.96	69.69	19.22
ELSA-D	2022-12-14 22:52:12	545.83	69.69	19.20
STARLINK-3078	2022-12-15 02:01:24	574.41	69.68	19.28
STARLINK-3077	2022-12-15 00:30:00	574.96	69.76	19.25
ZHUHAI-1 OHS-01	2022-12-15 09:12:36	490.41	69.63	19.15
JIADING 1	2022-12-15 06:21.48	479.79	69.54	19.25
JILIN-01-07	2022-12-14 18:09:12	544.92	69.66	19.12
COSMOS 1805	2022-12-14 17:45:48	519.06	69.72	19.33
STARLINK-3085	2022-12-14 23:27:24	573.73	69.59	19.36
STARLINK-3051	2022-12-14 22:55:24	575.31	69.46	19.13
JIADING 1	2022-12-15 06:21:48	479.51	69.55	19.26
SPACEBEE-139	2022-12-15 10:59:12	484.25	69.35	19.33

B

Code

This Appendix contains the scripts developed for the analysis performed in this thesis. Listing B.1 contains the script that was previously developed for EISCAT UHF meteor analysis and modified in this work to analyse satellites that were measured during the operation of the radar and also perform analysis to find the offset in EISCAT UHF range. This work was started during the project paper work, and continued and concluded in this thesis. Listing B.2 contains the script developed for the analysis of EISCAT UHF and MAARSY data presented in this thesis.

```
#written by Devin Huyghebaert and Juha Vierinen
#Sept. 23, 2022

#modified by Sara Vaden for satellite detections
#spring 2024

#Software to read in converted EISCAT raw voltage data and
#perform meteor analysis on the results
#The EISCAT data is first converted to a Digital_RF friendly
#format in a separate step

import digital_rf as drf
import numpy as np
import numpy as n
import matplotlib.pyplot as plt
import h5py
import pandas as pd
import glob
import eiscat_decode
```

```
import scipy.constants as c
import os
import datetime
from pyproj import Transformer, CRS
import pytz
from skyfield.api import load, wgs84, EarthSatellite
import scipy.optimize as sio
import time
use_mpi=True
try:
    from mpi4py import MPI

    comm= MPI.COMM_WORLD
    size=comm.Get_size()
    rank=comm.Get_rank()
except:
    use_mpi=False



def sinc_model(x,meas_freq):
    a=x[0]
    f=x[1]
    L=x[2]
    sincf=(n.sin(n.pi*L*(meas_freq-f+1e-9))/(n.pi*(meas_freq-f
    +1e-9)))**2.0
    sincf=sincf/n.max(sincf)
    return( a*sincf )


def fit_sinctop(meas_freq,meas_pwr,L=122*1.2e-6):
    """
    fit a sinc to the ambiguity function to get a better
    frequency resolution
    """
    f0=n.mean(meas_freq)
    a0=n.max(meas_pwr)

    def model(x):
        return(sinc_model(x,meas_freq))

    def ss(x):
        fm=model(x)
        s=n.sum(n.abs(fm-meas_pwr)**2.0)
        return(s)
    xhat=sio.fmin(ss,[a0,f0,L])
    xhat=sio.fmin(ss,xhat)
    return(xhat)


def analyze_hour(year=2022,month=12,day=13,hour=11,minute=9,
    second=35, txdir='/urdr/data/digital_rf_data/manda/uhf_tx',
     rxdir='/urdr/data/digital_rf_data/manda/uhf_rx', plot=
    False, plot_ambiguity=True, plot_sincfit=False,
```

```
    snr_threshold=25, meteor_output_directory="meteor_output"):
69
70      # Notes from the manda vhf tarlan file (manda-v.tlan)
71      # tx pulse leading edge is at 73 us
72      # tx pulse trailing edge is at 219.4 us
73      # pulse length is 146.4 us, bit length is 2.4 us, 61 bits
74      # sample spacing is 1.2 us
75      # note that the transmit samples start at 73.6 us, not at
        73 us
76      #
77      # the signal reception starts at 343 us and ends at 1473.4
        us, giving 942 samples
78      # the IPP is 1500 us.
79      # noise injection between 1473.4 to 1497 microseconds
80      #
81      # start tx sampling at 73.6 us
82      # at 343 us, reception occurs
83      # there should thus be a 269.4 us additional offset applied
         to the range gate that an echo is observed at
84
85      os.system("mkdir -p %s"%(meteor_output_directory))
86
87      #---
88      #TX read
89      #---
90
91      #find all tx files within directory
92      f_tx=glob.glob(f"{txdir}/{int(year):04d}_{int(month):02d}_{
        int(day):02d}_{int(hour):02d}/*")
93
94      #sort the TX files in time based on filename
95      f_tx.sort()
96
97
98      #take the first file for the TX and obtain the TX pulse
        samples and #timing
99      tx_file = h5py.File(f_tx[0],'r')
100     tx_pulse_samples = tx_file['tx_pulse_samples'][...]
101     tx_pulse_timing = tx_file['tx_pulse_timing'][...]
102
103     #only use 122 TX samples
104     tx_pulse_samples = tx_pulse_samples[:,:,5:127]
105
106     #---
107
108     #---
109     #RX read
110     #---
111
112     #sample rate and sample type for experiment
113     #1.2 us baud for receiver samples
114     sample_rate = np.float128(1/1.2e-6)
115     sample_dtype = np.dtype([('r','<i2'),('i','<i2')])
116
```

```
117     #create read object for experiment to look at using
        DigitalRF
118     read_object = drf.DigitalRFReader(rxdir)
119
120     #find the bounds for the RX samples
121     start_index,end_index = read_object.get_bounds(f'{year:04d
        }{month:02d}{day:02d}_{hour:02d}')
122
123     #determine the number of ranges to analyze
124     range_num = 750
125
126     n_fft_stage1=128
127     # decimation performed at the first stage with the C
        program
128     decimation = 1.0
129
130     # range index 0 would correspond to this range in km, this
        should be
131     # determined from the tarlan file.
132     minimum_range = 270e-6*c.c/2.0/1e3
133
134     # check from tarlan, probably not exactly correct.
135     radar_freq=930e6
136
137     #calculate the total number of samples per cycle (128
        pulses)
138     samples_per_code_cycle = int(128*.0015*sample_rate+0.5)+
        range_num
139
140     iono_file_create=0
141
142     #cycle through the TX files (correspond to 4.8 second
        integration #periods for MANDA)
143     start_t= int(12.5*(minute+(second/60)))
144
145     # if wanting plots for the entire duration of the satellite
        , use these
146     range_inx,doppler_inx,time_h,time_m,time_s,time_ms,
        interpol_range,t,interpol_doppler,snr_value
        =[],[],[],[],[],[],[],[],[],[]
147
148     for tx_file_num in range(start_t,start_t+2 ,size):
149         #for saving the data to HDF5
150         hdf5_times = []
151         hdf5_doppler = []
152         hdf5_length = []
153         hdf5_psl = []
154         hdf5_range = []
155         hdf5_snr = []
156         hdf5_phase = []
157         hdf5_cross_spectra = []
158
159         sec =(f_tx[tx_file_num][-8:-3])
160
```

```
        # if wanting plots for each file, use these
        doppler_val,snr_value,range_inx,doppler_inx
        =[],[],[],[]

        #read in transmit samples and timing for current file,
        3read in only the files where
        #there is possible satellites
        tx_file = h5py.File(f_tx[tx_file_num],'r')
        tx_pulse_samples = tx_file['tx_pulse_samples'][...]
        tx_pulse_timing = tx_file['tx_pulse_timing'][...]

        #offset is due to how EISCAT saves the TX samples -
        #in reality there are 122 baud,
        #but EISCAT saves 128
        tx_pulse_samples = tx_pulse_samples[:,:,5:127]
        tx_pulse_samples = np.asarray(tx_pulse_samples,
        dtype=np.complex64)

        file_t0=tx_pulse_timing[1,0]

        #save time for timing of processing
        start_time = time.time()

        #for each file there are 25 128 pulse sequences.
        #Loop through all 25
        for code_seq in range(25):

            # if wanting plots for every pulse sequence,
            #use these. (128 loops before plot)
            doppler_inx,range_inx,time_h,time_m,time_s,
            time_ms,interpol_range,t,interpol_doppler
            = [],[],[],[],[],[],[],[],[]

            #determine the start index of the first RX sample
            #(tx pulse plus start range)
            #satellite range found from tle used here, 540km
            tx_start_index = int((tx_pulse_timing
            [1,code_seq*128]+((540000*2)/c.c))*sample_rate+0.5)

            pd_time = (pd.to_datetime(int(tx_pulse_timing
            [1,code_seq*128]*1000), utc=True, unit='ms'))

            try:
                #read in data from both RX channels
                #(channels 0,1). This is for VHF
                rx_data1 = read_object.read(tx_start_index,
                tx_start_index+samples_per_code_cycle,
                f'{year:04d}{month:02d}{day:02d}_{hour:02d}')
                rx_data1 = np.asarray(rx_data1[tx_start_index]
                ['r']+1.0j*rx_data1[tx_start_index]['i'],
                dtype=np.complex64)
            except:
                #print('Read Out of Bounds, skipping')
                break
```

```
215
216             #record time for reading in samples
217             time1=time.time()
218
219             #perform an initial decode to find times
220             #with meteors.  This is performed for all data.
221             c_code_output = eiscat_decode.eiscat_decode
222             (np.copy(rx_data1),
223             np.conj(tx_pulse_samples[0,:,:]))
224
225             # hard coded range gates 0 to 750
226             F = np.fft.fftshift(np.abs(np.fft.fft(c_code_output
227             [:750,:,:],n_fft_stage1,axis=2))**2.0,axes=2)
228             N_fft_1=122.0
229
230             # noise floor estimate, 0.67449 is median absolute
231             #deviation
232             noise_floor_estimate=np.median(F)/0.67449
233             noise_floor_estimate2=np.mean(F)
234
235             # calculate signal to noise ratio
236             snr = (F-noise_floor_estimate)/
237             noise_floor_estimate
238
239             #find the max value for each pulse in
240             #range-Doppler space
241             #This provides an initial estimate for pulses to
242             #look further into for meteors
243             max_snr_for_pulse = np.amax(snr,axis=(0,2))
244             max_p_for_pulse = np.amax(F,axis=(0,2))
245
246             for pulse_num in range(128):
247                 # if signal to noise ratio is higher than
248                 #threshold empirically determined
249                 if max_snr_for_pulse[pulse_num]>snr_threshold:
250
251                     #plotting max snr for every pulse
252                     #over threshold
253                     #plt.figure(figsize=(14,12))
254                     #plt.imshow(snr[:,pulse_num,:],
255                     aspect='auto',origin='lower')
256                     #plt.title('SNR')
257                     #plt.xlabel('Doppler')
258                     #plt.ylabel('Range')
259                     #plt.show()
260
261                     # finding the time for the pulse
262                     pulse_time_pd = (pd.to_datetime((int
263                     (tx_pulse_timing[1,code_seq*128]*1000)),
264                     utc=True, unit='ms'))
265                     time_s.append(pulse_time_pd.second)
266                     time_ms.append(pulse_time_pd.microsecond)
267                     time_m.append(pulse_time_pd.minute)
268                     time_h.append(pd.Timestamp.to_pydatetime
```

```
(pulse_time_pd))

#meteor analysis
#find the index where the maximum occurs
#in range-Doppler space for the pulse

ind = np.unravel_index(np.argmax(snr
[:,pulse_num,:]),snr[:,pulse_num,:].shape)
doppler_inx.append(ind[1])
range_inx.append(ind[0])


# iterpolation
max_inx = np.argmax(np.amax(
snr[:,pulse_num,:],axis=1),axis=0)
#copy the rx and tx samples
#for interpolation
rx=np.copy(rx_data1[(pulse_num*1250):
((pulse_num+1)*1250),0])
tx=np.zeros(1250,dtype=np.complex64)
tx[0:122]=np.conj(tx_pulse_samples
[0,pulse_num,:])

#interpolate the rx and tx samples in time
xp=np.arange(1250)*1.2e-6
interp_factor=20
ixp=np.arange(interp_factor*1250)*
1.2e-6/interp_factor

irx=np.interp(ixp,xp,rx)
itx=np.interp(ixp,xp,tx)

#easy to modify values for
#the interpolation
course_rg=max_inx
tx_len=122
fft_factor=50

#create array to store interpolated
#range-Doppler spectra
interp_fft_array = np.zeros((4*
interp_factor,fft_factor*tx_len*
interp_factor),dtype=np.complex64)

#calculate the range-Doppler values with
#the interpolation
highres_rgs=np.arange(course_rg*
#interp_factor -2*
interp_factor,course_rg*interp_factor +
2*interp_factor)

for ri,range_idx in enumerate(highres_rgs):
    interp_fft_array[ri,:] = (np.fft.
    fftshift(np.fft.fft(irx[(range_idx):
```

```
323                     (range_idx+interp_factor*tx_len)]*np.
324                     conj(itx[0:(tx_len*interp_factor)]),
325                     fft_factor*interp_factor*tx_len)))
326
327                 #find the maximum range-Doppler index with
328                 #the interpolation
329                 interp_pwr=np.abs(interp_fft_array)**2.0
330
331                 snr2=(((N_fft_1**2.0)*np.max(interp_pwr)/
332                 ((tx_len*interp_factor)**2.0))-
333                 noise_floor_estimate)/noise_floor_estimate
334
335
336                 max_interp_idx=np.unravel_index(np.argmax
337                 (interp_pwr),interp_fft_array.shape)
338                 rg_max=(course_rg*interp_factor +
339                 max_interp_idx[0])
340
341                 # this is the fresp of the maximum
342                 #range gate.
343                 interp_fvec=n.fft.fftshift(n.fft.fftfreq
344                 (interp_factor*fft_factor*tx_len,d=1.0/
345                 (interp_factor*sample_rate)))
346                 dop_max=max_interp_idx[1]
347                 max_pwr_rg=n.abs(interp_fft_array
348                 [max_interp_idx[0],:])**2.0
349                 mpr=n.max(max_pwr_rg)
350
351                 # fit a sinc function to the peak of
352                 #the ambiguity function to get a
353                 # better doppler estimate
354                 xhat=fit_sinctop(interp_fvec[(dop_max-10):
355                 (dop_max+10)],max_pwr_rg[(dop_max-10):
356                 (dop_max+10)])
357                 sincfit_doppler=xhat[1]
358
359                 if plot_sincfit:
360                     fv=n.linspace(-10e3,10e3,num=10000)
361                     model_fv=fv+interp_fvec[dop_max]
362                     model_pwr=sinc_model(xhat,model_fv)
363                     plt.plot(interp_fvec,max_pwr_rg,"o")
364                     plt.plot(model_fv,model_pwr)
365                     plt.axvline(interp_fvec[dop_max])
366                     plt.axvline(xhat[1],color="red")
367                     plt.xlim([xhat[1]-3e3,xhat[1]+3e3])
368                     plt.show()
369
370
371                 # 2*f*v/c = c*df/2/f
372                 dopplerzp = np.fft.fftshift(np.fft.fftfreq
373                 (fft_factor*interp_factor*tx_len,
374                 d=1.2e-6/interp_factor))*c.c/930e6/2.0
375
376                 interpol_doppler.append(dopplerzp[dop_max])
```

```
377
378                 sincfit_dop=c.c*sincfit_doppler/
379                 2.0/radar_freq
380
381                 # new range estimate from interpolation
382                 interp_range_est=((rg_max - 2*
383                 interp_factor)*1.2e-6*c.c/
384                 (interp_factor*2.0)/1000+540)
385                 interpol_range.append(interp_range_est)
386
387                 #append the values for the current meteor
388                 #detected for saving to HDF5
389                 hdf5_times.append(pulse_time_pd)
390                 # get from sincfit
391                 hdf5_doppler.append(sincfit_dop)
392                 hdf5_length.append(xhat[2])
393                 hdf5_range.append(interp_range_est)
394                 hdf5_psl.append(sidelobe_pwr_ratio)
395                 # get from high res fit
396                 hdf5_snr.append(snr2)
397                 hdf5_phase.append(np.angle(
398                 interp_fft_array[max_interp_idx]/
399                 interp_factor))
400
401             #write HDF5 file here for the meteor
402             if len(hdf5_times)>0:
403                 output_fname="%s/match_function-%1.2f.h5"%
404                 (meteor_output_directory,file_t0)
405                 print("writing %s"%(output_fname))
406                 meteor_values_file=h5py.File(output_fname,'w')
407
408                 # date and experiment
409                 meteor_values_file.create_dataset('date',
410                 data=[year,month,day])
411
412                 meteor_values_file.create_dataset(f'time',
413                 data=np.asarray(hdf5_times))
414                 meteor_values_file.create_dataset(f'doppler',
415                 data=np.asarray(hdf5_doppler))
416                 meteor_values_file.create_dataset
417                 (f'ambiguity_length',
418                 data=np.asarray(hdf5_length))
419                 meteor_values_file.create_dataset(f'range',
420                 data=np.asarray(hdf5_range))
421                 meteor_values_file.create_dataset(f'snr',
422                 data=np.asarray(hdf5_snr))
423                 meteor_values_file.create_dataset(f'psl',
424                 data=np.asarray(hdf5_psl))
425                 meteor_values_file.create_dataset(f'phase',
426                 data=np.asarray(hdf5_phase))
427
428                 meteor_values_file.close()
429
430
```

```
431     # connecting radar range with satellite TLE range
432
433     if len(doppler_inx)>1:
434                 plt_range=c.c*np.array(range_inx)/
435                 sample_rate/2/1e3 + (540)
436
437                 print('Radar range:',np.sum(plt_range)/
438                 len(plt_range))
439                 print('Interpol range:', np.sum(interpol_range)
440                 /len(interpol_range))
441
442                 # plotting satellite range
443                 ts = load.timescale()
444                 tromso = [19.230422,69.586552,86]
445
446                 # tle for the current satellite searched for
447                 TLE = """STARLINK-4334
448 1 53665U 22105T   22347.74129335 -.00000957  00000-0 -69927-4
449 0  9997
450 2 53665  97.6590 226.4854 0002071  45.7667 314.3727 15.01262577
451 15907"""
452                 name, L1, L2 = TLE.splitlines()
453
454                 # put in epoch from TLE
455                 epoch_h = 6+(54/60)+((10/60)/60)
456
457                 hours = np.linspace(epoch_h-10, (epoch_h)+10,
458                 len(plt_range))
459                # epoch day, hours array to get entire orbit,
460                #len is the radar range to have the same
461                #number of points
462                 times = ts.utc(year, month, day, hours)
463
464                 # create satellite object from TLE and
465                 #time array
466                 satellite = EarthSatellite(L1, L2, name, ts)
467                 geocentrics = satellite.at(times)
468                 subpoints = wgs84.subpoint_of(geocentrics)
469                 heights = wgs84.height_of(geocentrics).km
470
471                 # transform latitude and longitude coordinates
472                 #into geocentric coordinates
473                 crs1 = CRS(proj='geocent',ellps='WGS84')
474                 crs2 = CRS(proj='latlong',ellps = 'WGS84')
475                 transformer = Transformer.from_crs(crs2,crs1)
476                 station_x, station_y, station_z = transformer.
477                 transform(tromso[0],tromso[1],tromso[2],
478                 radians=False)
479                 # define the coordinates for the radar site
480                 eiscat =(station_x, station_y,station_z)
481
482                 tz = pytz.timezone('UTC')
483
484                 # caltulate the distance between the radar site
```

```
485                 #and every point in satellite orbit
486                 distances = []
487                 time_sat = []
488                 h = []
489                 for t, lat, lon, heigh in zip(times,subpoints.
490                 latitude.degrees,subpoints.longitude.
491                 degrees,heights):
492                     # transform the coordintates for the
493                     #satellite orbit
494                     sat_x,sat_y,sat_z = transformer.transform
495                     (lon,lat,heigh*10**3, radians=False)
496                     # find the distance
497                     dist = np.sqrt((eiscat[0]-(sat_x))**2+
498                     (eiscat[1]-(sat_y))**2+
499                     (eiscat[2]-(sat_z))**2)
500                     distances.append(dist*10**(-3))
501                     time_sat.append(t.astimezone(tz))
502                     h.append(heigh)
503
504                 # create timestamps to compare times from
505                 #radar with times from satellite orbit
506                 timestamp1 = np.array([dt.timestamp()for
507                 dt in time_h])
508                 timestamp2 = np.array([dt.timestamp()for
509                 dt in time_sat])
510                 time_diff = timestamp2 - timestamp1
511                 print('Satellite range:',np.sum(distances)/
512                 len(distances))
513
514                 # shift the radar times to match
515                 #the satellite times
516                 new_time_h = []
517                 for i in np.arange(0,len(time_h)):
518                     new_time_h.append(time_h[i] +
519                     datetime.timedelta(seconds=0.6))
520
521                 # ignore different objects than meteor presents
522                 #in the radar detections
523                 new_interpol_range = []
524                 av_interpol = sum(interpol_range)/
525                 len(interpol_range)
526                 for indx in interpol_range:
527                     if indx > av_interpol +100:
528                         new_interpol_range.append(av_interpol)
529                     else:
530                         new_interpol_range.append(indx)
531
532                 # find difference between radar interpolated
533                 #radar range and tle range
534                 diff = [abs(di-p_r)for di, p_r in
535                 zip(distances,new_interpol_range)]
536                 print('difference:', sum(diff)/len(diff))
537
538
```

```
if __name__ == "__main__":
    # put in time from the closest approach time collected for
    satellite tle data
    year = int(2022)
    month = int(12)
    day = int(14)
    minute = int(54)
    second = int(3)
    for hour in range(6,7):

        datadir=f"/urdr/data/digital_rf_data/manda/uhf_rx/"

        txdir=f"/urdr/data/digital_rf_data/manda/uhf_tx/"

        #print("%s %s %s %s"%(year,month,day,hour))
        analyze_hour(year=year,month=month,day=day,hour=
        int(hour), minute=int(minute),second=int(second),
                    txdir=txdir,
                    rxdir=datadir,
                    snr_threshold=100,
                    plot_ambiguity=False,
                    meteor_output_directory="/home/sarav/
                    eiscat_sat_detect/manda_sat_detect_uhf")
```

Listing B.1: *Satellite analysis*

```
import numpy as np
import h5py
import matplotlib.pyplot as plt
import datetime
import pyproj
import math
import os
import scipy.optimize as so
import matplotlib.dates as mdates
warnings.filterwarnings('ignore')
import jcoord_juha as jcoord    #coordinate transformations
import glob
import antenna                  #eiscat uhf beam pattern
import scipy


# import file with all meteor data
f = h5py.File('all_meteors.h5','r')

# assign variables to the different keys
meteor_numbers = f['meteor_numbers'][:]
doppler = f['doppler'][:]
range = f['range'][:]
snr = f['snr'][:]
time = f['time'][:]


def ecef_to_llh(x,y,z):
```

```
    """
    transform between cartesian coordinates and to latitude,
    longitude,
    altitude coordinates

    Args:
    x, y, z = cartesian coordinates, ecef (earth-centered
    earth-fixed), represente position relative to center
    of the reference ellipsoid

    Returns:
    lat, lon, alt = llh ellipsoidal coordinates,
    expressed in latitude and longitude and height relative
    to ellipsoidal model of earth
    """
    transformer = pyproj.Transformer.from_crs(
    {"proj":'geocent',"ellps":'WGS84',"datum":'WGS84'},
    {"proj":'latlong',"ellps":'WGS84',"datum":'WGS84'})

    lon,lat,alt = transformer.transform(x,y,z,radians = False)
    return [lat,lon,alt]


def llh_to_ecef(radar_loc):
    """
    transform between radar location in lon, lat, alt to
    cartesian coordinates, x, y, z

    Args:
    radar_loc = radar location represented in llh coordinates
    (lat, lon, alt)

    Returns:
    x,y,z = radar location in ecef (cartesian coordinates)
    in km when /1000
    """
    transformer = pyproj.Transformer.from_crs
    ({"proj":'latlong',"ellps":'WGS84',"datum":'WGS84'},
    {"proj":'geocent',"ellps":'WGS84',"datum":'WGS84'})
    x, y, z = transformer.transform(radar_loc[1], radar_loc[0],
    radar_loc[2], radians = False)
    return [x/1000, y/1000, z/1000]



def scatter_location_determination(rx_lat_lon_alt,
    tx_lat_lon_alt, rf_path, azi, elev):
    """
    Given a distance, elevation, azimuth, recevier location
    and transmitter location, generate the lat, lon, alt
    of the point assuming straight line propagation

    Args:
    rx_lat_lon_alt = radar receiver location
```

```
    in lat, lon, alt coordinates
    tx_lat_lon_alt = radar transmitter location
    in lat, lon, alt coordinates
    rf_path = the distance from the radar transmitter
    to the object observed
    azi = azimuth of the radar during experiment
    elev = elevation of the radar during experiment

    Return:
    scat_lat_lon_alt_conv = latitude, longitude, altitude
    of the object
    """

    # what is this
    scatter_altitude = 110.0

    # azimuth and elevation in radians
    azi = azi*np.pi/180
    elev = elev*np.pi/180

    # sin and cos of the radar coordinates in radians
    slat = np.sin(rx_lat_lon_alt[0]*np.pi/180)
    slon = np.sin(rx_lat_lon_alt[1]*np.pi/180)
    clat = np.cos(rx_lat_lon_alt[0]*np.pi/180)
    clon = np.cos(rx_lat_lon_alt[1]*np.pi/180)


    # transforming radar coordinates to cartesian coordinates
    rx_x,rx_y,rx_z = llh_to_ecef(rx_lat_lon_alt)
    tx_x,tx_y,tx_z = llh_to_ecef(tx_lat_lon_alt)

    # finding the distance between the transmitter and receiver
    rx_tx_d = np.sqrt((rx_x-tx_x)**2+(rx_z-tx_z)**2+
    (rx_z-tx_z)**2)


    # determine if the receiver and transmitter are in the same
    #location (monostatic vs bistatic)
    if rx_tx_d==0:
        r_rs_d = rf_path/2.0
        if (elev<0).any():
            rx_re = np.sqrt(rx_x**2+rx_y**2+rx_z**2)
            elev = (np.arccos(((scatter_altitude+rx_re)**2-
            rx_re**2-r_rs_d**2)/(-2*rx_re*r_rs_d))-(np.pi/2))

    else:
        # if the radar is bistatic, use geometry to determine
        #the distance from the receiver to
        #the scattering location
        # not included in this work
        pass


    scat_xyz = np.zeros((len(elev),3),dtype=np.float32)
```

```
135
136     # azi and elev in south east zenith (up) corrdinates,
137     #unit vectors * the one way distance of the radar beam
138     south = -np.cos(azi)*np.cos(elev)*r_rs_d
139     east = np.sin(azi)*np.cos(elev)*r_rs_d
140     zenith = np.sin(elev)*r_rs_d
141
142     # calculating x,y,z from spherical coordinates times
143     #the couth, east, zenith vector
144     # more explanation in the thesis
145     scat_xyz[:,0] = rx_x + (slat * clon * south) + (-slon *
146     east) + (clat * clon * zenith)
147     scat_xyz[:,1] = rx_y + (slat * slon * south) + ( clon *
148     east) + (clat * slon * zenith)
149     scat_xyz[:,2] = rx_z + (-clat *south) + (slat*zenith)
150
151
152     # get lat, lon coordinates from the cartesian coordinates
153     scat_lat_lon_alt = ecef_to_llh(scat_xyz[:,0]*1000.0,
154     scat_xyz[:,1]*1000.0, scat_xyz[:,2]*1000.0)
155
156     scat_lat_lon_alt_conv = np.zeros((len(elev),4),
157     dtype=np.float32)
158
159     scat_lat_lon_alt_conv[:,0] = (scat_lat_lon_alt[:][0])
160     scat_lat_lon_alt_conv[:,1] = (scat_lat_lon_alt[:][1])
161     scat_lat_lon_alt_conv[:,2] = (scat_lat_lon_alt[:][2])
162     /1000.0
163     scat_lat_lon_alt_conv[:,3] = r_rs_d
164
165
166     return scat_lat_lon_alt_conv
167
168
169
170
171 # radar locations
172 # lat (deg), lon (deg), alt (m)
173 eiscat_uhf = [69.5864,19.2257,93]
174 maarsy_loc = [69.2984,16.0413,4]
175
176 eiscat_diameter = 32        #[m]
177 eiscat_wavelength = 0.322   #[m]
178 eiscat_peak_gain = 48.1     #[dBi]
179
180 # eiscat
181 elevation = 37     # [deg]
182 azimuth = 257.1    # [deg]
183
184
185 # emtpy lists for use later
186 m_alt,m_snr,maarsy_alt,maarsy_snr,m_doppler,maarsy_dop,
187 maarsy_time,m_time,result=[],[],[],[],[],[],[],[],[]
188 diff_ablated_m,simple_ablated,fragment,heights_abl=[],[],[],[]
```

```
189
190 # settings for bigger text size when plotting
191 small_size =  14
192 medium_size = 29
193 bigger_size = 38
194
195 plt.rc('font',size =small_size)
196 plt.rc('axes', titlesize=medium_size)
197 plt.rc('axes', labelsize =medium_size)
198 plt.rc('xtick', labelsize=small_size)
199 plt.rc('ytick', labelsize = small_size)
200 plt.rc('legend', fontsize = small_size)
201 plt.rc('figure', titlesize=bigger_size)
202
203 # loop through all the meteors found in the eiscat uhf data,
204 #one at the time
205 for meteor in np.arange(0,len(np.unique(meteor_numbers))-1):
206     # meteor is now meteor numbers, not including -1,
207     meteor_range = range[meteor_numbers==meteor]
208     meteor_time = time[meteor_numbers==meteor]
209     meteor_snr = snr[meteor_numbers == meteor]
210     meteor_doppler = doppler[meteor_numbers == meteor]
211
212     # only including meteor events with enough information
213     if len(meteor_range) > 10:
214
215         # create eiscat beam vector
216         signal_angle = np.asarray([np.ones(len(meteor_range))*
217         elevation, np.ones(len(meteor_range))*azimuth])
218
219         # distance signal travels
220         rf_distance = (meteor_range*2)
221
222         # meteor location code, output in lat, lon, alt
223         data_loc = scatter_location_determination(eiscat_uhf,
224         eiscat_uhf,rf_distance, signal_angle[0,:],
225         signal_angle[1,:])
226
227         meteor_lat = data_loc[:,0]
228         meteor_lon = data_loc[:,1]
229
230         # finding the index for maximum snr and using for
231         #determining altitude, doppler and time
232         ind = meteor_snr.argmax()
233         m_alt.append(data_loc[:,2][ind])
234         m_snr.append(max(meteor_snr))
235         m_doppler.append(abs(meteor_doppler[ind]))
236         m_time.append(meteor_time[ind])
237
238
239         # Gaussian fit to the snr function
240         snr_curve = np.array(10.0*np.log10(meteor_snr))
241
242         time_m = np.array(meteor_time)
```

```
243         time_m= time_m.astype('float64')
244         time_vector =(np.vectorize(datetime.datetime.
245         utcfromtimestamp))
246         time_m =(time_vector(time_m))
247 
248         time_fit = np.array([(date-time_m[0]).total_seconds()
249         for date in time_m])
250 
251         n = len(snr_curve)
252         mean = sum(snr_curve*time_fit)/n
253         sigma = np.sqrt(sum(snr_curve*(time_fit-mean)**2/
254         sum(snr_curve)))
255 
256         def gaus(x,a,x0,sigma):
257             return a*np.exp(-(x-x0)**2/(2*sigma**2))
258 
259         popt,pcov = so.curve_fit(gaus,time_fit,snr_curve,
260         p0=[max(snr_curve),mean,sigma], maxfev =1000000)
261 
262         # estimating the meteors that could be located inside
263         #maarsy radar beam
264         var = 0.05
265         if maarsy_loc[1]-var < np.average(meteor_lon) <
266         maarsy_loc[1]+var and maarsy_loc[0]-var <
267         np.average(meteor_lat) < maarsy_loc[0]+var:
268             ind_maarsy = meteor_snr.argmax()
269             maarsy_alt.append(data_loc[:,2][ind_maarsy])
270             maarsy_snr.append(max(meteor_snr))
271             maarsy_dop.append(abs(meteor_doppler[ind_maarsy]))
272             maarsy_time.append(meteor_time[ind_maarsy])
273 
274             # using the gaussian curve fit for the events in
275             #maarsy beam
276             curve_fit = gaus(time_fit, *popt)
277             # difference bettween fit and original
278             difference = snr_curve - curve_fit
279             # gradient of the difference
280             grad = np.gradient(difference)
281 
282             # gradient is used to classify differential
283             #ablation meteor events
284 
285             avg = sum(grad)/len(grad)
286             avg_diff = sum(difference)/len(difference)
287 
288             n = 0
289             ablated_heights = []
290             for i in np.arange(0,len(grad)):
291                 if np.abs(grad[i])> avg+2:
292                     n += 1
293                     ablated_heights.append(data_loc[:,2][i])
294 
295             # calculating the fft of the difference to find
296             #the fragmented events
```

```
297             diff = np.fft.fftshift(np.fft.fft(difference))
298             shifted_k = np.fft.fftshift(np.fft.fftfreq
299             (len(diff))*len(diff))
300             trap =(np.abs(np.trapz(diff, shifted_k)))
301
302             if 2 < n <= 7:
303                 # event classified as differential ablation
304                 diff_ablated_m.append(data_loc[:,2]
305                 [ind_maarsy])
306                 # the height when the meteor experience
307                 #differential ablation
308                 heights_abl.append(np.mean(ablated_heights))
309
310             elif n ==0 and trap > 10:
311                 # event classified as simple abaltion
312                 simple_ablated.append(data_loc[:,2]
313                 [ind_maarsy])
314
315             elif trap < 10:
316                 # event classified as fragmentation
317                 fragment.append(data_loc[:,2][ind_maarsy])
318
319
320
321
322 # -------- MAARSY and EISCAT radar analysis -----------
323
324 # from this point the maarsy data is included in the analysis
325
326
327 # fit a 2nd order polynomial to x, y, and z coordinates
328 for meteor trajectory
329 #used later for angle calculations
330 def fit_meteor_trajectory(t,x,y,z):
331     n_m=len(t)
332     A=np.zeros([n_m,3])
333     A[:,0]=1.0
334     A[:,1]=t
335     A[:,2]=t**2.0
336
337     x_par=np.linalg.lstsq(A,x, rcond = -1)[0]
338     y_par=np.linalg.lstsq(A,y, rcond = -1)[0]
339     z_par=np.linalg.lstsq(A,z, rcond = -1)[0]
340
341     def xfun(t):
342         return(x_par[0]+x_par[1]*t+x_par[2]*t**2.0)
343     def yfun(t):
344         return(y_par[0]+y_par[1]*t+y_par[2]*t**2.0)
345     def zfun(t):
346         return(z_par[0]+z_par[1]*t+z_par[2]*t**2.0)
347
348     return(xfun,yfun,zfun)
349
350
```

```
m_alt,m_snr,maarsy_alt,maarsy_snr,m_doppler,maarsy_dop,
maarsy_time,m_time,result,a_maarsy_alt,a_maarsy_snr,
a_maarsy_dop = [],[],[],[],[],[],[],[],[],[],[],[]

# eiscat meteors
file = h5py.File('all_meteors.h5',"r")

meteor_numbers = file['meteor_numbers'][:]
doppler = file['doppler'][:]
range_e = file['range'][()]
snr = file['snr'][:]
time = file['time'][()]
time= time.astype('float64')

# maarsy meteors
fm = glob.glob("/mnt/data/juha/maarsy/2023/12/202312*.h5")
fm.sort()

# radar locations in ECEF coordiantes
ecef_eiscat = jcoord.geodetic2ecef(eiscat_uhf[0],
eiscat_uhf[1], eiscat_uhf[2])
ecef_maarsy = jcoord.geodetic2ecef(maarsy_loc[0],
maarsy_loc[1], maarsy_loc[2])

# eiscat beam unit vector
eiscat_k_vec = jcoord.azel_ecef(eiscat_uhf[0],
eiscat_uhf[1], eiscat_uhf[2], azimuth, elevation)


difference,difference_cali,meteor_count,eiscat_count,
possible_count,heights_abl,abl_vel =
[],[],[],[],[],[],[]

# loop through the maarsy files
for i in fm:
    try:
        h = h5py.File(i, "r")
    except:
        continue

    # check if the measurement is good
    #(contains enough elements)
    if len(h.keys())> 36:
        n_good = len(h["gidx"][()])
    else:
        continue
    if n_good < 2:
        continue

    # find meteor positions in maarsy data
    t0=h["t0"][()]
    ipp_time=h["gidx"][()]*1e-3
    time_maarsy=t0+ipp_time
    north=-h["pos_e"][()]
```

```
405     east=-h["pos_n"][()]
406     up=h["pos_u"][()]
407     snr_m=h['snr'][()]
408     snr_time = t0 + 0.001*h["t_idx"][()]
409     if "fit_rcs_vec" in h.keys():
410         rcs_m = h["fit_rcs_vec"]
411 
412     # normalize time for later use
413     t_mean = np.mean(time_maarsy)
414     t_normalized = time_maarsy - t_mean
415 
416     # meteor position in ECEF coordinates
417     ecef_meteor=jcoord.enu2ecef(maarsy_loc[0],maarsy_loc[1],
418     maarsy_loc[2], east, north, up)
419 
420     # add maarsy position to the meteor position
421     ecef_meteor[0,:]+= ecef_maarsy[0]
422     ecef_meteor[1,:]+= ecef_maarsy[1]
423     ecef_meteor[2,:]+= ecef_maarsy[2]
424 
425     # find range between eiscat and maarsy meteor position
426     range_eiscat = np.sqrt((ecef_meteor[0,:]-
427     ecef_eiscat[0])**2.0+(ecef_meteor[1,:]-
428     ecef_eiscat[1])**2.0+(ecef_meteor[2,:]-
429     ecef_eiscat[2])**2.0)
430 
431     # make a fit to the meteor vectors, less noise
432     #in calculation
433     p_e2m=np.copy(ecef_meteor)
434     p_e2m[0,:]=ecef_meteor[0,:]-ecef_eiscat[0]
435     p_e2m[1,:]=ecef_meteor[1,:]-ecef_eiscat[1]
436     p_e2m[2,:]=ecef_meteor[2,:]-ecef_eiscat[2]
437 
438     p_e2mx,p_e2my,p_e2mz=fit_meteor_trajectory(t_normalized,
439                                                p_e2m[0,:],
440                                                p_e2m[1,:],
441                                                p_e2m[2,:])
442     # check if fit is good
443     if False:
444         plt.plot(t_normalized,p_e2m[0,:],".")
445         plt.plot(t_normalized,p_e2mx(t_normalized))
446         plt.plot(t_normalized,p_e2m[1,:],".")
447         plt.plot(t_normalized,p_e2my(t_normalized))
448         plt.plot(t_normalized,p_e2m[2,:],".")
449         plt.plot(t_normalized,p_e2mz(t_normalized))
450         plt.show()
451 
452     # find indexes where eiscat measurements
453     #overlap with maarsy
454     overlap_idx=np.where( (time > (np.min(time_maarsy)-1)) &
455     ((time < (np.max(time_maarsy)+1))))[0]
456     # maarsy meteor geodetic coordinates
457     lat_meteor, lon_meteor, h_meteor = jcoord.ecef2geodetic
458     (ecef_meteor[0,:], ecef_meteor[1,:], ecef_meteor[2,:])
```

```
    h_meteor = h_meteor/1000

    # calibration factor to eiscat range determined from
    #emiprical analysis of data
    calibration_factor = 0.830355894

    degree = 1
    # if a overlapping meteor event is found,
    #containing enough values for analysis
    if len(overlap_idx)>0 and meteor_numbers[overlap_idx][0]
    != -1 and len(range_e[overlap_idx])>10:
        # find the times for meteor detection in eiscat
        start_time =(time[overlap_idx][0]).astype('float64')
        end_time = (time[overlap_idx][-1]).astype('float64')

        time_start = (time_vector(start_time))
        time_end = (time_vector(end_time))
        time_diff = (time_end - time_start)/2
        middle_time = time_start + time_diff
        meteor_count.append(middle_time)

        # trajectory fit to maarsy and eiscat trajectory
        coefficients_m = np.polyfit(time_maarsy,
        range_eiscat/1e3, degree)
        poly_func_m = np.poly1d(coefficients_m)

        coefficients_e = np.polyfit(time[overlap_idx],
        range_e[overlap_idx], degree) #-calibration_factor
        poly_func_e = np.poly1d(coefficients_e)

        avg_diff = sum(poly_func_e(time[overlap_idx]))/
        len(poly_func_e(time[overlap_idx]))-
        sum(poly_func_m(time_maarsy))/
        len(poly_func_m(time_maarsy))
        avg_diff_cali = sum(poly_func_e(time[overlap_idx])-
        calibration_factor)/len(poly_func_e(time[overlap_idx])-
        calibration_factor)-sum(poly_func_m(time_maarsy))/
        len(poly_func_m(time_maarsy))
        if np.abs(avg_diff_cali) < 3:
            difference_cali.append(avg_diff_cali)
            difference.append(avg_diff)

        # plot of ranges with their fit to make sure
        #they overlap
        plt.plot(time_vector(time_maarsy), poly_func_m
        (time_maarsy), label ='maarsy fit', color = 'green' )
        plt.plot(time_vector(time[overlap_idx]),
        poly_func_e(time[overlap_idx]), label ='eiscat fit',
        color = 'blue' )
        plt.plot(time_vector(time_maarsy), range_eiscat/1e3,
        "o", markersize = 10,label ='maarsy', color = 'green')
        plt.plot(time_vector(time[overlap_idx]), range_e
        [overlap_idx], "o",markersize = 10, label ='eiscat',
        color= 'blue')
```

```
513         plt.xticks(rotation=10)
514         plt.xlabel('Time (UTC)')
515         plt.ylabel('Range (km)')
516         plt.title('{t1}, {t2}'.format(t1 = time_vector(t0),
517         t2 = time_vector(time[overlap_idx][0])))
518         plt.title('Meteor range')
519         plt.legend()
520         plt.show()
521
522         signal_angle = np.asarray([np.ones(len(range_e
523         [overlap_idx]))*azimuth, np.ones(len(range_e
524         [overlap_idx]))*elevation])
525         rf_distance = ((range_e[overlap_idx]-
526         calibration_factor)*2)
527         data_loc = scatter_location_determination(eiscat_uhf,
528         eiscat_uhf,rf_distance, signal_angle[0,:],
529         signal_angle[1,:])
530
531         ind = snr[overlap_idx].argmax()
532         a_maarsy_alt.append(data_loc[:,2][ind])
533         a_maarsy_snr.append(max(snr[overlap_idx]))
534         a_maarsy_dop.append(abs(doppler[overlap_idx][ind]))
535
536         # normalize eiscat time
537         e_t_normalized=time[overlap_idx]-t_mean
538
539         # calculate normalized position vector for
540         #maarsy detections at eiscat observation times
541         # when maarsy and eiscat overlap
542         p_e2m_len=np.sqrt(p_e2mx(e_t_normalized)**2.0+p_e2my
543         (e_t_normalized)**2.0+p_e2mz(e_t_normalized)**2.0)
544         p_e2m_overlap=np.zeros([3,len(e_t_normalized)])
545         p_e2m_overlap[0,:]=p_e2mx(e_t_normalized)/p_e2m_len
546         p_e2m_overlap[1,:]=p_e2my(e_t_normalized)/p_e2m_len
547         p_e2m_overlap[2,:]=p_e2mz(e_t_normalized)/p_e2m_len
548         antenna_boresight_angles=np.arccos(p_e2m_overlap[0,:]*
549         eiscat_k_vec[0]+p_e2m_overlap[1,:]*eiscat_k_vec[1]+
550         p_e2m_overlap[2,:]*eiscat_k_vec[2])
551
552         # same but for maarsy detection times
553         p_e2m_len=np.sqrt(p_e2mx(t_normalized)**2.0+
554         p_e2my(t_normalized)**2.0+p_e2mz(t_normalized)**2.0)
555         p_e2m_m=np.zeros([3,len(t_normalized)])
556         p_e2m_m[0,:]=p_e2mx(t_normalized)/p_e2m_len
557         p_e2m_m[1,:]=p_e2my(t_normalized)/p_e2m_len
558         p_e2m_m[2,:]=p_e2mz(t_normalized)/p_e2m_len
559
560         # angle meteor differs away from eiscat main beam
561         antenna_boresight_angles_m=np.arccos(p_e2m_m[0,:]*
562         eiscat_k_vec[0]+p_e2m_m[1,:]*eiscat_k_vec[1]+
563         p_e2m_m[2,:]*eiscat_k_vec[2])
564         # calculate eiscat gain at the angle found
565         gain = antenna.eiscat_uhf_fun(antenna_boresight_angles)
566
```

```
567         # calculate eiscat rcs when variables contains enough
568         #values for analysis
569         if 10*np.log10(gain)[0] >10 and np.abs(avg_diff) < 2
570         and "fit_rcs_vec" in h.keys():
571             # calculate eiscat rcs
572             T_sys = 100                             #[K]
573             P_t = 1.2e6                             #[W]
574             bandwidth = 1/146.4e-6                  #[Hz]
575             noise = scipy.constants.Boltzmann*
576             T_sys*(bandwidth)                       #[W]
577             P_r = noise*snr[overlap_idx]            #[W]
578             R = ((range_e[overlap_idx]-
579             calibration_factor)*1e3)                #[m]
580
581             rcs = (((4*np.pi)**3)*(R**4)*P_r)/(P_t*(gain**2)*
582             (eiscat_wavelength**2))
583
584             # find the differential ablated heights using rcs
585             n= 0
586             ablated_heights = []
587             vel_ablated = []
588             for grad in np.arange(0, len(rcs)):
589                 if np.abs(np.gradient(10*np.log10(rcs))
590                 [grad]) > 2:
591                     n += 1
592                     ablated_heights.append(data_loc[:,2][grad])
593                     vel_ablated.append(doppler[overlap_idx]
594                     [grad])
595
596             if 1 < n < 4:
597                 heights_abl.append(np.mean(ablated_heights))
598                 abl_vel.append(np.mean(vel_ablated))
599
600 # histograms for altitude, snr and doppler for eiscat, possibly
        maarsy and maarsy
601 if True:
602     m_alt = np.array(m_alt)/1000
603     maarsy_alt = np.array(maarsy_alt)/1000
604     a_maarsy_alt=np.array(a_maarsy_alt)/1000
605     alt_bins = np.linspace(math.ceil(min(m_alt)), math.floor(
        max(m_alt)),40)
606     plt.hist(m_alt, bins=alt_bins, histtype='step', lw = 3, ec=
        'blue', label = 'EISCAT')
607     plt.hist(maarsy_alt, bins=alt_bins, histtype='step',lw = 3,
        ec= 'red', label = 'Estimated dual')
608     plt.hist(a_maarsy_alt, bins=alt_bins, histtype='step', lw =
        3,ec= 'green', label = 'Found dual')
609     plt.title('Meteor altitude')
610     plt.xlabel('Altitude (km)')
611     plt.ylabel('Meteor counts')
612     plt.legend()
613     plt.show()
614
615     maarsy_snr = 10.0*np.log10(maarsy_snr)
```

```
616     m_snr = 10.0*np.log10(m_snr)
617     a_maarsy_snr = 10.0*np.log10(a_maarsy_snr)
618     snr_bins = np.linspace(math.ceil(min(m_snr)), math.floor(
        max(m_snr)),40)
619     plt.hist(m_snr, bins=snr_bins, histtype='step',lw = 3, ec=
        'blue', label = 'EISCAT')
620     plt.hist(maarsy_snr, bins=snr_bins, histtype='step', lw =
        3,ec= 'red', label = 'Estimated dual')
621     plt.hist(a_maarsy_snr, bins=snr_bins, histtype='step', lw =
         3,ec= 'green', label = 'Found dual')
622     plt.title('Meteor SNR')
623     plt.xlabel('SNR (dB)')
624     plt.ylabel('Meteor counts')
625     plt.legend()
626     plt.show()
627
628
629     dop_bins = np.linspace(math.ceil(min(m_doppler)), math.
        floor(max(m_doppler)),40)
630     plt.hist(m_doppler, bins=dop_bins, histtype='step',lw = 3,
        ec= 'blue', label = 'EISCAT')
631     plt.hist(maarsy_dop, bins=dop_bins, histtype='step',lw = 3,
         ec= 'red', label = 'Estimated dual')
632     plt.hist(a_maarsy_dop, bins=dop_bins, histtype='step', lw =
         3,ec= 'green', label = 'Found dual')
633     plt.title('Meteor doppler velocity')
634     plt.xlabel('Doppler (km/s)')
635     plt.ylabel('Meteor counts')
636     plt.legend()
637     plt.show()
```

Listing B.2: *EISCAT and MAARSY analysis*